Hydrodynamics of Fringing-Field Induced Defects in Nematic Liquid Crystals

Richard James,[1] Eero Willman,[1] Rami Ghannam,[2] Jeroen Beeckman,[3] and F. Aníbal Fernández[1]
[1)] *University College London, Torrington Place, London WC1E 7JE, U.K.*
[2)] *James Watt School of Engineering, University of Glasgow, G12 8QQ, U.K.*
[3)] *Ghent University, Technologiepark-Zwijnaarde 126, 9052 Ghent, Belgium.*

(*Electronic mail: rwjames@gmail.com)

(Dated: 25 August 2021)

Consumer demand for high resolution and high refresh-rate displays has naturally led to the fabrication of liquid crystal displays with ever smaller pixels. As a consequence, fringing fields between adjacent pixels grow in magnitude, leading to abrupt changes in orientation. Electric field strengths above some threshold can lead to order melting and in turn disclinations. This paper presents accurate modelling of disclinations induced by fringing fields due to interdigitated electrodes in a nematic liquid crystal calculated by means of the Landau-de Gennes theory. Disclination paths are resolved taking into account the flow of the liquid crystal. Making use of interdigitated electrodes, precise electrical control over the creation and positioning of defects is demonstrated for homeotropic, planar, hybrid and in-plane surface alignments.

I. INTRODUCTION

As liquid crystal displays increase in resolution and complexity there is a tendency for defects to form in the liquid crystal layer, induced by strong electric fields or geometrical features. Pixels are typically designed so as to avoid the formation of defects, which can be detrimental to image quality. Similarly, high pixel densities are demanded by non-display applications of liquid crystals, including holography and beam-steering[1]. Spatial Light Modulators (SLMs) for electrical hologram generation based on Liquid Crystal on Silicon (LCoS) panels are available[2] with pixel-pitches of $3.74\,\mu$m.

As pixels shrink, large electric fields can arise in the inter-pixel gap leading to order melting and disclinations in turn[3]. Disclinations can be of high density, playing an important and potentially advantageous role in device operation. Such fringing-field induced disclinations are the product of pincement, an effect which is well studied in liquid crystal cells with planar alignment[4–8] or in multi-domain structures[9]. For very high resolutions, pixels become narrow compared to the cell gap, which is fixed by the optical path length. Electrically driven reorientation is confined to the vicinity of the pixellated electrode, since the electric field extends only partially into the liquid crystal bulk.

Interdigitated electrodes are widely employed in In-Plane Switching (IPS) displays, with a typical electrode pitch of $\sim 12\,\mu$m, in excess of the cell gap[10]. Disclinations induced by fringing-fields due to interdigitated electrodes have been observed experimentally with homeotropic[11,12], in-plane[13] and hybrid[14] alignments as well as predicted theoretically[15,16]. Lindquist[11] demonstrated a phase grating formed by interdigitated electrodes with an electrode-pitch of $8\,\mu$m and reported the successful fabrication of a $0.8\,\mu$m device. Predominantly, these studies focus on the disclination structures that result at steady-state; however, the impact of the electrode spacing on the response time has also been assessed experimentally[12] with electrode pitches as small as $2\,\mu$m. Proposed applications include reconfigurable diffraction gratings[11,17,18] and fast switching displays[13,19] with typical[13] electrode-pitches of $8\,\mu$m or less. Additionally, such disclinations can be used to reconfigure liquid crystal colloids[14,20].

Colloidal particles are attracted to disclination lines, since they essentially exclude a volume of high energy should they decorate a line[21]. Small particles can be trapped within the saturn ring defect associated with a larger particle[21] or within disclinations arising in chiral-nematic filled wedge cells[22]. Defect networks induced by topologically patterned substrates have been shown to trap particles and are reconfigurable by external fields, affording control over particle position[23]. Recently, this trapping and positional control has been demonstrated by electrically induced defects due to crossed electrodes[24] and interdigitated electrodes (with hybrid alignment)[14]. Bacteria immersed in lyotropic liquid crystals can similarly be trapped and transported by defects[25].

In this paper the hydrodynamics of disclination formation by fringing fields due to interdigitated electrodes is studied theoretically. Conditions necessary to create disclinations are explored for homeotropic, planar, hybrid and in-plane surface alignments with both positive and negative dielectric anisotropy liquid crystals. Both the anchoring strength and device proportions have a profound influence on threshold voltages required to induce disclinations, as demonstrated in sections IX and X.

II. MODEL

Both orientation and order of the liquid crystal may be described by the nematic order tensor[4] $\mathbf{Q}$ which is traceless, so that it vanishes in the isotropic phase, and symmetric. A tensorial representation, over a purely vectorial one, is necessary to fully describe the biaxial ordering adopted by molecules in the vincity of defects. The Q-tensor may be defined as $\mathbf{Q} = S_1(3\hat{n}\otimes\hat{n} - I)/2 + S_2(3\hat{m}\otimes\hat{m} - I)/2$, where S_1 and S_2 represent the de-

gree of order about the orthogonal unit vectors $\hat{n}$ and $\hat{m}$ respectively. At equilibrium $\mathbf{Q}$ minimises the Landau-de Gennes free energy functional[4,26]

$$\mathcal{F}(\mathbf{Q},\partial\mathbf{Q}) \;=\; \int_\Omega f(\mathbf{Q},\partial\mathbf{Q})\,\mathrm{d}V + \int_\Gamma f_S(\mathbf{Q})\,\mathrm{d}S, \quad (1)$$

where $f(\mathbf{Q},\partial\mathbf{Q})$ is the free energy density given by

$$f(\mathbf{Q},\partial\mathbf{Q}) \;=\; f_D(\mathbf{Q},\partial\mathbf{Q}) + f_B(\mathbf{Q}) - f_E(\mathbf{Q}), \quad (2)$$

and comprises elastic, $f_D(\mathbf{Q},\partial\mathbf{Q})$; bulk, $f_B(\mathbf{Q})$; and electrostatic, $f_E(\mathbf{Q})$, free-energy densities defined as

$$\begin{aligned} f_B(\mathbf{Q}) =& \tfrac{1}{2}A\,Q_{\alpha\beta}Q_{\beta\alpha} + \tfrac{1}{3}B\,Q_{\alpha\beta}Q_{\beta\gamma}Q_{\gamma\alpha} \\ &+ \tfrac{1}{4}C\,(Q_{\alpha\beta}Q_{\beta\alpha})^2, \quad (3)\\ f_D(\mathbf{Q},\partial\mathbf{Q}) =& \tfrac{1}{2}L_1\,\partial_\gamma Q_{\alpha\beta}\partial_\gamma Q_{\alpha\beta} + \tfrac{1}{2}L_2\,\partial_\beta Q_{\alpha\beta}\partial_\gamma Q_{\alpha\gamma} \\ &+ \tfrac{1}{2}L_3\,\partial_\gamma Q_{\alpha\beta}\partial_\beta Q_{\alpha\gamma} \\ &+ \tfrac{1}{2}L_6\,Q_{\alpha\beta}\partial_\alpha Q_{\mu\nu}\partial_\beta Q_{\mu\nu}, \quad (4)\\ f_E(\mathbf{Q}) =& \tfrac{1}{2}\varepsilon_0\partial_\alpha u\,\varepsilon_{\alpha\beta}\,\partial_\beta u - P_\alpha\partial_\alpha u. \quad (5) \end{aligned}$$

Summation over repeated indices is assumed. Here A, B and C are material bulk constants; L_1, L_2, L_3 and L_6 are elastic constants; $\varepsilon_{\alpha\beta}$ is the permittivity tensor; u is the electric potential, found by minimising the electrical energy $\int_\Omega f_E(\mathbf{Q})\mathrm{d}V$ with respect to u; and P_α is the flexoelectric polarisation[27]

$$P_\alpha = \xi_1\partial_\beta Q_{\alpha\beta} + \xi_2 Q_{\alpha\beta}\partial_\gamma Q_{\beta\gamma}. \quad (6)$$

The surface free energy density,

$$f_S(\mathbf{Q}) = a\,Q_{\alpha\beta}Q_{\beta\alpha} + W_1\,\xi_\alpha Q_{\alpha\beta}\xi_\beta + W_2\,\zeta_\alpha Q_{\alpha\beta}\zeta_\beta, \quad (7)$$

allows for different azimuthal and zenithal anchoring strengths[28]. Coefficients W_1 and W_2 are anchoring strengths and the unit vectors $\hat{\xi}$, $\hat{\zeta}$ and the preferred alignment direction are orthogonal. The order parameter at the surface is controlled by the coefficient a.

Dynamic evolution of the Q-tensor is governed by

$$J\ddot{Q}_{\alpha\beta} = h_{\alpha\beta} + h'_{\alpha\beta} - \lambda\delta_{\alpha\beta} - \epsilon_{\alpha\beta\gamma}\lambda_\gamma, \quad (8)$$

where $\epsilon_{\alpha\beta\gamma}$ is the Levi-Civita tensor and λ and λ_γ are Lagrange multipliers that enforce the zero trace and symmetry requirements of the Q-tensor. The moment of inertial density, J, is typically and herein assumed negligible[29–31]. The molecular field, $h_{\alpha\beta}$, is given by the first variation in $\mathcal{F}(\mathbf{Q},\partial\mathbf{Q})$

$$h_{\alpha\beta} = -\frac{\partial f}{\partial Q_{\alpha\beta}} + \partial_\gamma\frac{\partial f}{\partial\,(\partial_\gamma Q_{\alpha\beta})}. \quad (9)$$

The viscous molecular field, $h'_{\alpha\beta}$, is defined as[29]

$$-h'_{\alpha\beta} = \tfrac{1}{2}\mu_2 A_{\alpha\beta} + \mu_1 N_{\alpha\beta}, \quad (10)$$

$$N_{\alpha\beta} = \frac{\mathrm{d}Q_{\alpha\beta}}{\mathrm{d}t} + W_{\alpha\mu}Q_{\mu\beta} - Q_{\alpha\mu}W_{\mu\beta}, \quad (11)$$

where $A_{\alpha\beta} = \frac{1}{2}(\partial_\alpha v_\beta + \partial_\beta v_\alpha)$, $W_{\alpha\beta} = \frac{1}{2}(\partial_\alpha v_\beta - \partial_\beta v_\alpha)$ and the material derivative $\frac{\mathrm{d}}{\mathrm{d}t}$ is $\frac{\partial}{\partial t} + v_\gamma\partial_\gamma$.

Flow of the liquid crystal (assumed incompressible) is governed by the Navier-Stokes equation, written in terms of a generalised stress tensor

$$\rho\frac{\mathrm{d}v_\alpha}{\mathrm{d}t} = \partial_\beta\left(-p\,\delta_{\beta\alpha} + \sigma^d_{\beta\alpha} + \sigma^e_{\beta\alpha} + \sigma^v_{\beta\alpha}\right), \quad (12)$$

where ρ is the density, v_α is the velocity and p is the pressure. Three contributions to the overall stress tensor are considered[29]: the viscous stress, $\sigma^v_{\alpha\beta}$, the distortion stress, $\sigma^d_{\alpha\beta}$, and the Maxwell stress tensor, $\sigma^e_{\alpha\beta}$,

$$\begin{aligned} \sigma^v_{\alpha\beta} =& \beta_1 Q_{\alpha\beta}Q_{\mu\nu}A_{\mu\nu} + \beta_4 A_{\alpha\beta} + \beta_5 Q_{\alpha\mu}A_{\mu\beta} + \beta_6 Q_{\beta\mu}A_{\mu\alpha} \\ &+ \tfrac{1}{2}\mu_2 N_{\alpha\beta} - \mu_1 Q_{\alpha\mu}N_{\mu\beta} + \mu_1 Q_{\beta\mu}N_{\mu\alpha}, \quad (13)\\ \sigma^d_{\alpha\beta} =& -\frac{\partial f_D}{\partial(\partial_\alpha Q_{\mu\nu})}\partial_\beta Q_{\mu\nu}, \quad (14)\\ \sigma^e_{\alpha\beta} =& D_\alpha E_\beta - \tfrac{1}{2}D_\mu E_\mu\delta_{\alpha\beta}, \quad (15) \end{aligned}$$

where $E_\alpha = -\partial_\alpha u$ is the electric field and $D_\alpha = \varepsilon_0\varepsilon_{\alpha\beta}E_\beta + P_\alpha$ is the electric displacement.

In the limit of a constant order, the above formulation reduces to the Ericksen-Leslie theory. The more general variational theory proposed by Sonnet[32], reduces to an equivalent set of equations when the Rayleigh dissipation functional is restricted to be a bilinear form in $N_{\alpha\beta}$ and $A_{\alpha\beta}$ and up to quadratic order in $\mathbf{Q}$.

A. Numerical Details

A finite element approach is taken to solve the aforementioned set of partial differential equations[33,34], implemented in Matlab/C++. Weak forms and matrix equations that result are detailed in our previous work[33]. An overview of the methodology follows.

In the cases considered herein, reorientation of the liquid crystal is driven by the applied voltage. Thus, for the sake of stability, it is advantageous to take a monolithic approach in computing the Q-tensor and electric potential whereby the solution vector takes the form $\{q_1, q_2, q_3, q_4, q_5, u\}$, where $\mathbf{Q} = q_i\mathbf{T}_i$. Basis tensors, $\mathbf{T}_i$, satisfy the tracelessness and symmetry constraints of $\mathbf{Q}$[35]. Consequently, Lagrange multiplier terms in (8) may be dropped. Crank-Nicholson time stepping is employed with Newton-Raphson iterations within each time step to deal with the non-linearity of the governing equations. Velocity and pressure fields are solved for at the half time-step (consistently within each Newton iteration), so that the $\partial\mathbf{Q}/\partial t$ terms appearing in (12) can be evaluated by central differences, thus maintaining $O(\Delta t^2)$ accuracy of the Crank-Nicholson scheme. The steadiness approximation is made, whereby the time derivative of the velocity appearing in (12) is dropped and the velocity is assumed pseudo-steady with respect to $\mathbf{Q}$.

All variables, namely q_i, v_α and u, are discretised by second order triangular elements with the exception of

the pressure, for which first order elements are used in a mixed order scheme for the flow as a means to inhibit oscillatory pressure solutions. Adaptive meshing (h-adaptation) driven by an empirical error estimate derived from the free energy bar the electrostatic contribution serves to reduce the number of degrees of freedom. The time-step is dynamically adjusted to maintain a constant time-integration error[34], varying from $\sim 5\,\mathrm{ns}$ during nucleation to $\sim 0.2\,\mathrm{ms}$ near steady-state.

B. Material Properties

Material parameters of 5CB (at $25-26^{\circ}\mathrm{C}$)[36–40] are employed in the model. Bulk material constants are $\alpha = 0.13\times10^6\times(2/3)\,\mathrm{N/(m^2{\cdot}K)}$, $B=-1.6\times10^6\times(4/3)\,\mathrm{N/m^2}$ and $C=3.9\times10^6\times(4/9)\,\mathrm{N/m^2}$ with $A=\alpha(T-T^*)$, where T is the temperature and T^* is the supercooling temperature, the temperature beneath which the isotropic state is unstable. Elastic constants are $K_{11}=6.2\,\mathrm{pN}$, $K_{22}=3.9\,\mathrm{pN}$ and $K_{33}=8.2\,\mathrm{pN}$. In the case of strong anchoring the saddle-splay modulus, K_{24}, contributes a constant to the free energy and can be neglected. The relative permittivity perpendicular to the long molecular axis is $\varepsilon_\perp=7.0$ and the dielectric anisotropy is $\Delta\varepsilon=11.5$. Viscosity coefficients are $\gamma_1=0.0777\,\mathrm{Pa{\cdot}s}$, $\gamma_2=-0.0848\,\mathrm{Pa{\cdot}s}$, $\alpha_1=-0.0060\,\mathrm{Pa{\cdot}s}$, $\alpha_4=0.0652\,\mathrm{Pa{\cdot}s}$, $\alpha_5=0.0640\,\mathrm{Pa{\cdot}s}$ and $\alpha_6=-0.0208\,\mathrm{Pa{\cdot}s}$.

Elastic constants $\{L_1,L_2,L_3,L_6\}$ can be obtained from the splay, twist and bend elastic constants $\{K_{11},\ K_{22},\ K_{33},\ K_{24}\}$ using the expressions[41]

$$L_1=\tfrac{2}{27S_0^2}\left(K_{33}-K_{11}+3K_{22}\right), \tag{16}$$

$$L_2=\tfrac{4}{9S_0^2}\left(K_{11}-K_{22}-K_{24}\right), \tag{17}$$

$$L_3=\tfrac{4}{9S_0^2}K_{24}, \tag{18}$$

$$L_6=\tfrac{4}{27S_0^3}\left(K_{33}-K_{11}\right), \tag{19}$$

wherein the equilibrium value of the order parameter, S_0, is given by the stationary value of f_B with respect to S, yielding $S_0=(-B+\sqrt{B^2-24AC})/(6C)$. The permittivity tensor is defined $\varepsilon_{\alpha\beta}=\varepsilon_\perp\delta_{\alpha\beta}+\Delta\varepsilon\left[2Q_{\alpha\beta}/(3S_0)+\delta_{\alpha\beta}/3\right]$. In the limit of a constant order parameter the flexoelectric polarisation is equivalent to $\boldsymbol{P}=e_{11}\hat{n}(\nabla\cdot\hat{n})-e_{33}\hat{n}\times(\nabla\times\hat{n})$, yielding[27] $\xi_1=\frac{2}{9S_0}(e_{11}+2e_{33})$ and $\xi_2=\frac{4}{9S_0^2}(e_{11}-e_{33})$. Influence of the flexoelectric coefficients e_{11} and e_{33} is discussed in Sec. VIII, but elsewhere they are assumed zero.

Viscosity coefficients $\{\mu_1,\ \mu_2,\ \beta_1,\ \beta_4,\ \beta_5,\ \beta_6\}$ can be directly obtained from the Ericksen-Leslie coefficients $\{\alpha_1,\alpha_2,..,\alpha_6\}$ by means of the mappings[29]: $\mu_1=\frac{2}{9S_0^2}\gamma_1$, $\mu_2=\frac{2}{3S_0}\gamma_2$, $\beta_1=\frac{4}{9S_0^2}\alpha_1$, $\beta_5=\frac{2}{3S_0}\alpha_5$, $\beta_6=\frac{2}{3S_0}\alpha_6$ and $\beta_4=\alpha_4+S_0(\beta_5+\beta_6)/2$.

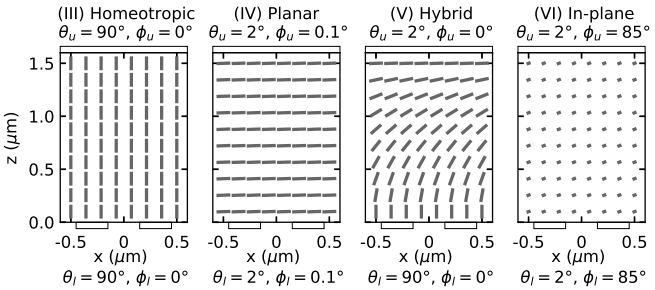

FIG. 1. Illustration of the surface alignment configurations analysed in sections III–VI, where grey line segments represent the starting director configurations (at time = 0) chosen for the simulations. Pre-tilt, θ, and pre-twist, ϕ, at the upper (u) and lower (l) alignment layer are indicated, where $\hat{n}=(\cos\theta\cos\phi,\cos\theta\sin\phi,\sin\theta)^T$.

C. Device description

A periodic structure with two interdigitated electrodes forms the modelling window, with a period of $1.2\,\mu$m and height of $1.6\,\mu$m, as depicted in Fig. 1. The electrode gap is set to match the electrode width of $0.3\,\mu$m. An upper electrode is included which offers an additional degree of control over the liquid crystal bulk. Due to the stretched aspect ratio of the device, the upper electrode has negligible influence on the electric field due to the interdigitated electrodes when grounded (unbiased).

The fabrication of interdigitated electrodes at these length scales is difficult but can, for example, be achieved using deep UV, X-ray or electron beam lithography techniques. In addition, similar switching mechanisms to those described herein are possible using the principle of fringe-field switching[13,19], whereby the same potential is applied to in-plane electrodes positioned above a dielectric layer seated on a ground plane, which reduces the risk of electrical shorts.

Non-slip boundary conditions are applied for the velocity. Unless otherwise stated $(T-T^*)=-2\,\mathrm{K}$ is assumed.

III. HOMEOTROPIC ALIGNMENT

Reorientation of a liquid crystal due to fringing-fields in a homeotropic cell is shown in Fig. 2. For simplicity of presentation, director streamlines are shown, whereby the director corresponds to the eigenvector associated with the largest eigenvalue of the Q-tensor. Prior to eigendecomposition, the Q-tensor is interpolated from the computational mesh, shown in Fig. 3, onto a regular grid to facilitate plotting. Initially, when a voltage is applied, the liquid crystal in the inter-pixel gap reorients towards the horizontal, giving rise to a bend-splay wall. For low applied voltages the core of the wall remains vertical and all changes in orientation are limited to a $\sim 0.3\mu$m thick layer above the lower alignment layer.

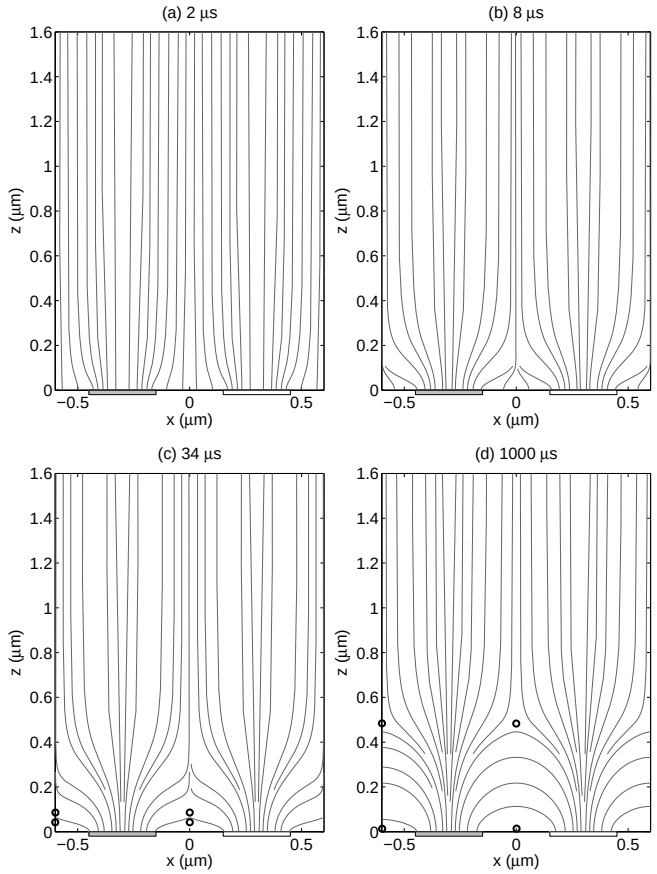

FIG. 2. Director streamlines depicting the switching dynamics of a homeotropic cell with interdigitated electrodes after applying ±3.97 V across the lower electrodes [the electrode positions are shown by rectangles that are shaded white for positive voltages (+3.97 V) and grey for negative (−3.97 V)]. Circles correspond to minima in S_1, i.e. disclinations, which form at 33 μs.

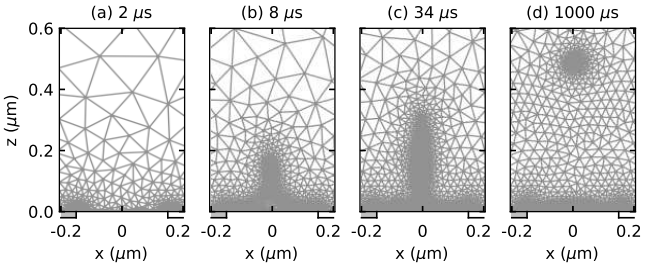

FIG. 3. Mesh in the vicinity of the electrode edges at four different times. Throughout the modelling window the element edge-length varies from 0.25 to 400 nm. Element count peaks at 34 μs with 8400 triangles.

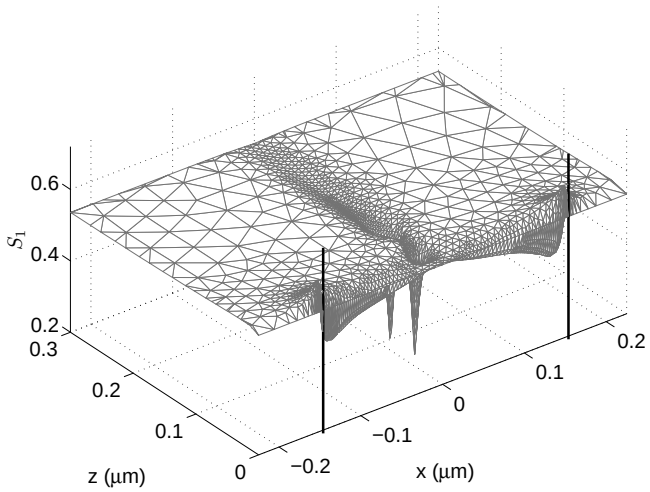

FIG. 4. Order parameter S_1 in the vicinity of the electrode edges at 34 μs, 1 μs after disclination formation. Dark lines show the positions of the electrode edges. Dips in order along $x = 0$ correspond to disclinations. The high electric field above the electrodes gives rise to an order parameter in excess of that of the bulk ($S_0 = 0.535$), which peaks above the electrode edges. Between electrodes the clash between the surface alignment and reorienting liquid crystal gives rise to a biaxial arrangement of liquid crystal and, correspondingly, a drop in S_1.

Increasing the applied voltage further compresses the wall, leading to a drop in order parameter and an increase in biaxiality within the wall. Above a specific value of applied voltage, ±3.97 V, there is an exchange of eigenvalues of the Q-tensor, giving rise to a ±1/2 disclination pair, as shown in Fig. 2 (c). This transformation from walls to disclination lines is known as pincement[4]. Throughout this paper this value of voltage will be referred to as the threshold voltage, U_{th}, and should not be confused with the Fréedericksz threshold. The applied voltage need only exceed the threshold voltage for a short time (33 μs for an applied voltage of ±3.97 V) to induce disclinations, after which a much reduced voltage is capable of separating the disclinations. Figure 4 shows the variation in order parameter at the same time, 1 μs after disclination formation, where the drop in order associated with the ±1/2 disclination lines is clearly visible.

Horizontal alignment between the disclination pairs is favoured due to the applied voltage, encouraging their separation. The +1/2 lines move downwards until becoming stationary 14 nm above the lower alignment layer whilst the −1/2 lines rise. A parallel can be drawn with growth of horizontal and vertical domains seen in the π cell, which are topologically distinct states and are separated by disclination lines. In a π cell, an applied voltage gives rise to a uniform vertical electric field in the liquid crystal layer. Disclinations separating coexisting horizontal and vertical domains move with a constant velocity that depends on the applied voltage[42]. In contrast, the use of interdigitated electrodes gives rise to an electric field that diminishes with distance within the liquid crystal layer, thus disclinations separate until the force due to the electric field matches the elastic attractive force.

Figure 5 (a) shows the paths disclinations follow when a voltage of ±3.97 V is applied, both with and without flow. Flow causes disclinations to form 14.6 μs earlier and

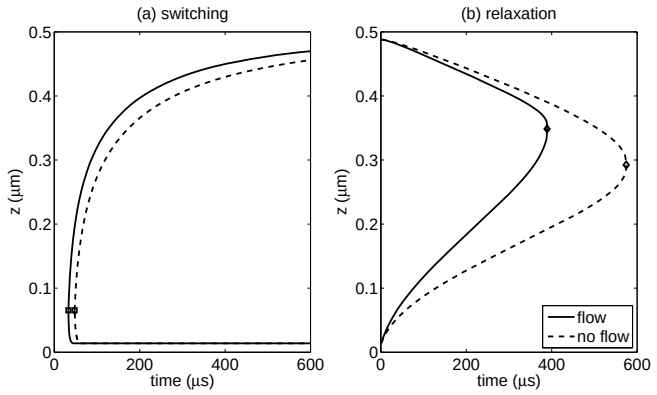

FIG. 5. Vertical disclination position as a function of time when (a) $\pm 3.97\,\mathrm{V}$ is applied and (b) the relaxation process that follows when the voltage is removed. Squares indicate nucleation points and diamonds annihilation points. If flow is neglected disclination creation is delayed by $14.6\,\mu$s.

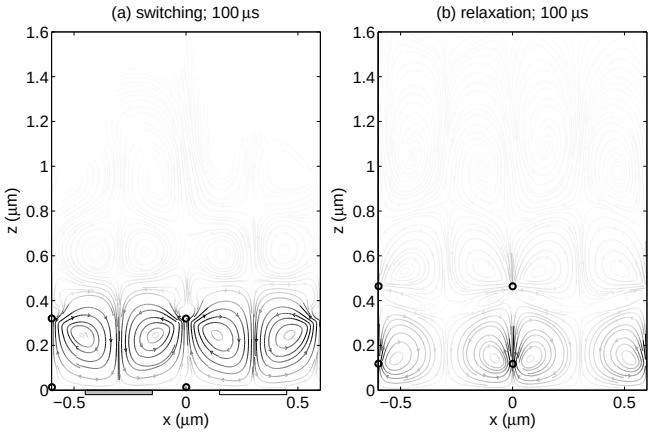

FIG. 6. Instantaneous velocity streamlines (a) 0.1 ms after applying $\pm 3.97\,\mathrm{V}$ and (b) 0.1 ms after relaxation from $\pm 3.97\,\mathrm{V}$. Streamline shade reveals the magnitude of the velocity field, with white and black corresponding to slow and fast flow respectively. During switching the velocity in the neighbourhood of the upper $-1/2$ lines has a maximum magnitude of $2.2 \times 10^{-4}\,\mathrm{ms}^{-1}$. During relaxation the velocity field peaks in magnitude at the lower $+1/2$ defect cores, with a maximum value of $3.5 \times 10^{-4}\,\mathrm{ms}^{-1}$.

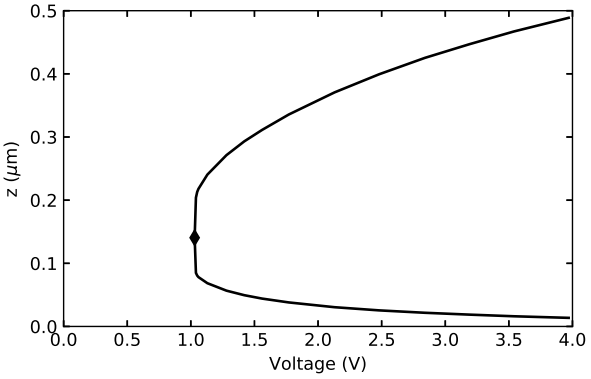

FIG. 7. Steady-state vertical position of $\pm 1/2$ disclinations as a function of voltage, as the applied voltage is reduced from $\pm 3.97\,\mathrm{V}$. Height is almost temperature invariant, but for the weak dependence of the permittivity on the order parameter.

accelerates their separation. Disclinations reach the same steady-state height of 488 nm after $\sim$ 2 ms both with and without flow. Figure 5 (b) shows the disclination trajectories when the applied voltage is removed. Confinement alters the behaviour in comparison to isolated disclination pairs[30,31]. When the voltage is removed, velocities of $+1/2$ and $-1/2$ disclinations differ markedly even if flow is neglected. Elastic distortion at the alignment layer expels the $+1/2$ disclinations away rapidly. As seen in the annihilation of isolated disclination pairs, both theoretically[30,31] and experimentally[43], here too the velocity field preferentially accelerates the $+1/2$ lines.

In Fig. 6 (a), the velocity field after applying $\pm 3.97\,\mathrm{V}$ for 0.1 ms is shown. At this time the $+1/2$ disclinations are already stationary above the lower alignment layer and have little influence on the velocity field. The $-1/2$ disclinations continue to rise and the velocity field near each disclination is in the positive z-direction and serves to compound the disclination velocity. Fig. 6 (b) shows the velocity field 0.1 ms after removing the voltage.

By varying the potential difference across the lower electrodes it is possible to control the vertical position of the $\pm 1/2$ disclinations, as shown in Fig. 7. When the voltage falls below $\pm 1.03\,\mathrm{V}$ the attractive elastic force overcomes the electric and the disclination lines annihilate to restore the starting vertical configuration. Disclinations annihilate at different locations than observed earlier in Fig. 5, where the applied voltage was removed abruptly. Gradually reducing the applied voltage serves to pin the $+1/2$ disclinations above the alignment layers, whilst the $-1/2$ disclinations descend. Relaxation may be accelerated by applying the same voltage to the interdigitated electrodes.

Varying the bias applied to the upper electrode provides a means to control the lateral separation of the $-1/2$ disclinations, as shown in Fig. 8 (b). The bias voltage augments the electric field at the nucleation point and hence a lesser voltage of $\pm 3.89\,\mathrm{V}$ is able to induce disclinations. Due to the lateral motion, flow now perturbs the disclination paths.

IV. PLANAR ALIGNMENT

In this section the disclination states induced with a planar alignment layer are studied. The surface director is chosen in the x-direction with a pre-tilt of $\theta_0 = 2°$, corresponding to antiparallel rubbing. A small pre-twist of $\phi_0 = 0.1°$ is chosen to allow in-plane reorientation of the liquid crystal to occur. When a voltage is applied, reorientation of the liquid crystal is most prominent above the centre of each electrode, where a bend-splay wall arises.

Provided the applied voltage is above some threshold,

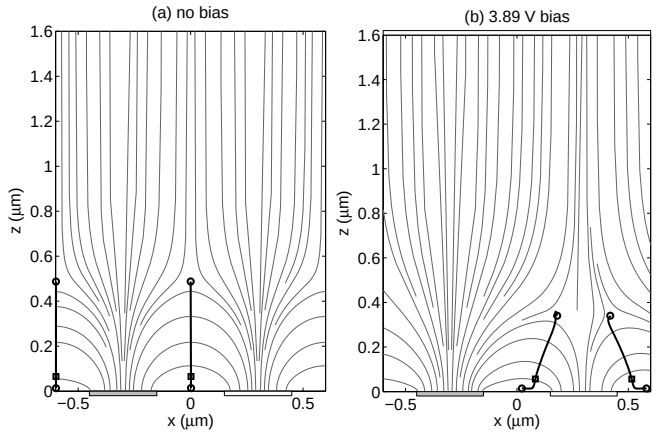

FIG. 8. Director streamlines at steady-state with homeotropic alignment. Black lines reveal trajectories followed by the disclinations and squares indicate nucleation points. In (a) ±3.97 V is applied to the lower electrodes with no bias to the upper electrode, whereas in (b) ±3.89 V is applied to the lower electrodes with a bias of +3.89 V to the upper electrode.

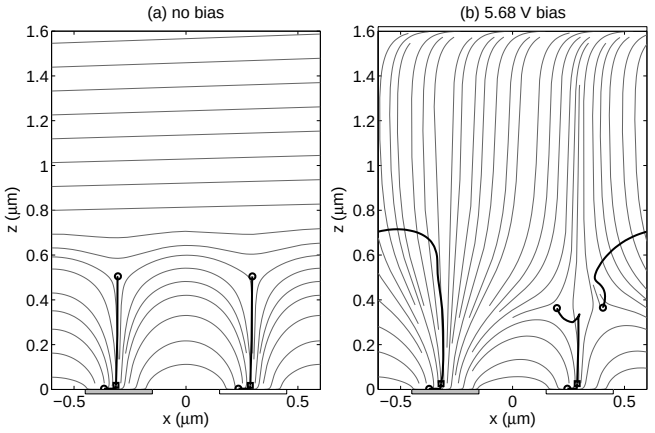

FIG. 9. Director streamlines at steady-state with planar alignment. In (a) ±5.19 V is applied to the lower electrodes and the upper electrode is grounded. Steady-state is reached after ∼ 2 ms. With a bias in (b), the approach to steady-state is slowed significantly, as the −1/2 lines migrate to the same height driven by their mutual repulsion (after 16 ms).

U_C, this bend-splay wall transforms into a twist wall. Thus, U_C provides a measure of the elastic anisotropy. Typically, $U_C \approx 2U_F$, where U_F is the Fréedericksz threshold, given by $U_F = \pi\sqrt{K_{11}/(\varepsilon_0\Delta\varepsilon)}$. The twist evolves at a rate determined by the director relaxation time[6] $\tau \sim \gamma_1\xi_E^2/\Delta K$. This depends on the electrical coherence length, $\xi_E = U_0\, d/U$, where $U_0 = \sqrt{K/(\varepsilon_0\Delta\varepsilon)}$, $K \sim (K_{11}+K_{33})/2$, U is the applied voltage, $d = 0.2\,\mu$m is the effective height of the wall and $\Delta K \sim (K_{11} + K_{33})/2 - K_{22}$ is the elastic anisotropy. Three factors are neglected in this approximation: flow of the liquid, which reduces τ; the influence of the pre-twist; and the change in electric potential due to reorientation (particularly if $\Delta\varepsilon$ is large), which reduces U_C. We find that, just below U_{th}, transformation to a fully twisted wall takes $\sim 20\,\mu$s.

If the applied voltage is ramped sufficiently slowly, twisting of the wall is complete, but for stepped voltages the transformation is merely partial when pincement occurs. Higher voltages are required to form disclinations from the more compact twist walls. Consequently, U_{th} differs for ramped and stepped voltage waveforms, taking the values ±5.41 V (for ramp rates of 55 mV/μs or less) and ±5.19 V respectively. If the pre-twist is increased, twist walls form more rapidly and U_{th} for a stepped waveforms tends to the ramped value (for example $U_{th} = \pm 5.36$ V with $\phi_0 = 1°$).

Applying a ±5.19 V voltage step gives rise to pairs of ±1/2 disclinations after 18 μs that form 12 nm to the left of the electrode-centre (a displacement due to the pretilt). As the disclinations diverge all twist that was once associated with the walls is lost. The director configuration shown in Fig. 9 (a) results at steady-state, where planar orientation persists in the bulk.

When a bias voltage is applied to the upper electrode (that matches the potential of the positive lower electrode) it serves to augment or diminish the electric field above alternate fingers of the lower electrodes. Contrary to the homeotropic case considered earlier, the voltage thresholds differ for alternate fingers, taking values of ±3.92 V and ±5.68 V. At steady-state Fig. 9 (b) results, where ±5.68 V has been applied to induce defects above both electrodes. Disclinations form above the centre of the electrodes, but the left-hand one rises higher and faster than the right. It moves beyond the left-hand edge of the modelling window and wraps around to the right, due to the periodic boundary condition, yielding finally the steady-state of Fig. 9 (b).

Choosing splayed alignment characteristic of the π cell yields almost identical results both with and without a bias voltage. After disclination formation, despite the initial splay, the defects support above them an almost planar, splay free layer. The twisted nematic case, with in-plane alignment at the upper alignment layer, also behaves similarly. Disclinations support above them a twisted layer. With a bias, the twist in the bulk is lost.

V. HYBRID ALIGNMENT

Hybrid Aligned Nematic (HAN) cells are constructed from a layer of liquid crystal sandwiched between two differently treated substrates; one yields homeotropic alignment and the other planar. Two possibilities exist with regards to the location of the interdigitated electrodes. If planar alignment is chosen near these electrodes switching proceeds much as it did for the planar cell, as shown in Fig. 9. Disclinations form above the centre of each electrode and again the −1/2 lines move upwards. There is some lateral movement associated with these disclinations, due to the vertical change in the tilt throughout the structure, but this movement ceases when disclinations are positioned above the electrode edge. The bulk

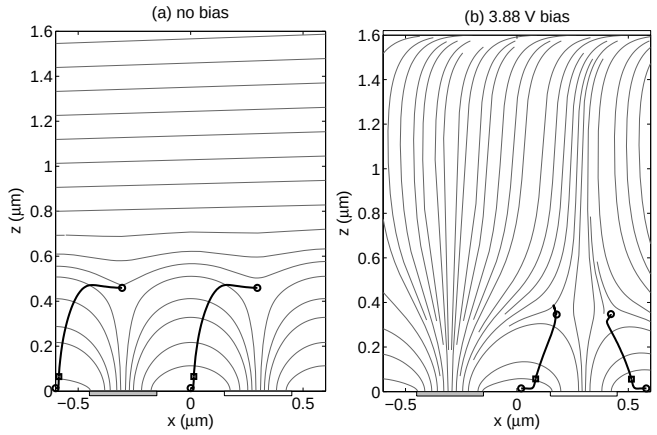

FIG. 10. Director streamlines at steady-state with hybrid alignment. Homeotropic anchoring is chosen at the lower alignment layer and planar at the upper. In (a) ±3.96 V is applied to the lower electrodes without bias to the upper electrode, whereas in (b) ±3.88 V is applied to the lower electrodes and +3.88 V to the upper.

arrangement of molecules remains in the HAN state.

Choosing homeotropic alignment above the interdigitated electrodes yields more interesting results. The pretilt is fixed at 90° and 2° at the lower and upper alignment layers respectively. If the applied voltage is below the threshold voltage of ±3.96 V, switching is confined to a small region above the lower alignment layer, as was seen in the homeotropic case. Voltages in excess of this threshold induce disclinations at the same positions as in the homeotropic cell, above the mid-point between the two electrodes. However, after forming, the −1/2 disclinations not only move upwards but laterally too.

As the disclinations continue to rise they also rotate until the situation shown in Fig. 10 (a) is reached after 16 ms. It takes longer to reach steady-state than the homeotropic cell as this rotation is driven by the elastic force from the bulk. Disclinations have facilitated transformation of the bulk from a hybrid to a planar state.

The voltage can be increased or decreased and the thickness of the planar region can be controlled. If the applied voltage is reduced to ±0.8 V or below the ±1/2 lines move until they are almost at the same vertical position and then move laterally before finally annihilating.

A single voltage threshold exists that gives rise to two disclination pairs within the modelling window with a bias applied, ±3.88 V. Fig. 10 (b) shows the resulting director field at stead-state, where the left-hand disclination forms sooner than the right.

VI. IN-PLANE ALIGNMENT

In-plane switching, due to its wide viewing angle characteristics, is commonly employed in displays. Consistent reorientation of the liquid crystal is ensured by the rubbing direction, which is typically a few degrees relative

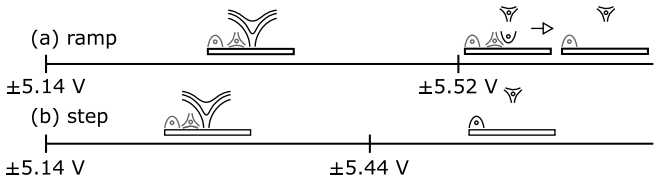

FIG. 11. Disclination and wall arrangements observed above one electrode with in-plane alignment. Horizontal axis represents the voltage, with threshold voltages labelled. In (a) the applied voltage is ramped, in (b) a step voltage is applied.

to the electrode edge. For the purposes of simulation this pre-twist angle is chosen as $\phi_0 = 85°$ (relative to x) and the pre-tilt is 2°. Even low applied voltages (far below U_{th}) are sufficient to rapidly rotate the molecules by almost $\pi/2$ above the lower alignment layer, giving rise to an almost planar alignment (along x) in this region. Reorientation proceeds into the bulk, resulting in an almost linearly twisted bulk. By changing the applied voltage the amount of twist can be controlled. This defect-free mode is attractive for display applications.

For larger applied voltages, the resulting disclination configuration depends on the exact voltage waveform applied, as sketched in Fig. 11. In case (a), as the voltage is ramped, a twist wall forms above the centre of each electrode, but additionally a region of biaxiality arises above the left-hand electrode edge. As the voltage is ramped beyond ±5.14 V, the biaxial region splits into two twist disclinations: a +1/2 line that remains stationary at the electrode edge and a −1/2 line that moves rightwards to the electrode centre. Above ±5.52 V the central wall undergoes pincement, giving rise to a +1/2 line that annihilates with the −1/2 line created previously. A −1/2 line from the wall remains, that rises upwards. In case (b), a step voltage is applied. Similarly to (a), a biaxial region forms above the left-hand electrode edge, but now the twist wall forms further left, nearby the biaxial region (a shift that depends on the pre-twist, tending to electrode edge for $\phi_0 = 88.2°$). Between ±5.14 V and ±5.44 V the biaxial region splits into disclinations whilst the wall migrates to the electrode centre. Above ±5.44 V the wall undergoes pincement rapidly, before it can move rightwards significantly. The lower +1/2 line settles above the left-hand electrode edge whilst the −1/2 line migrates diagonally up and rightwards.

As the −1/2 lines rise due to the electric field, they lose a portion of their twist, whilst the layer beneath them twists towards x. Above the disclinations the bulk becomes a linearly twisted layer, but this process is a slow one. Figure 12 (a) shows the steady-state liquid crystal orientation obtained ∼ 10 ms after applying a ±5.44 V voltage step. By changing the applied voltage the thickness of the $\pi/2$ twisted layer can be controlled.

When a bias voltage is applied to the upper electrode, there exist two threshold voltages for creating disclinations, as was observed for planar alignment. These thresholds are ±3.95 V and ±6.04 V. Fig. 12 (b) shows

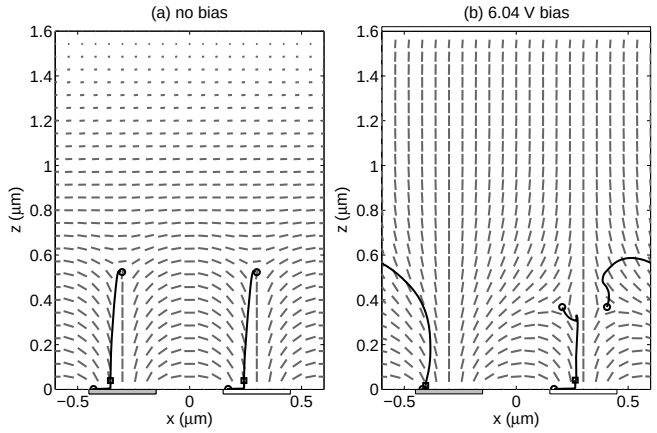

FIG. 12. Director field at steady-state with in-plane alignment (a) without and (b) with a bias voltage applied to the upper electrode. In (a) a linearly $\pi/2$ twisted bulk sits atop the disclinations, whereas in (b) the twist is lost.

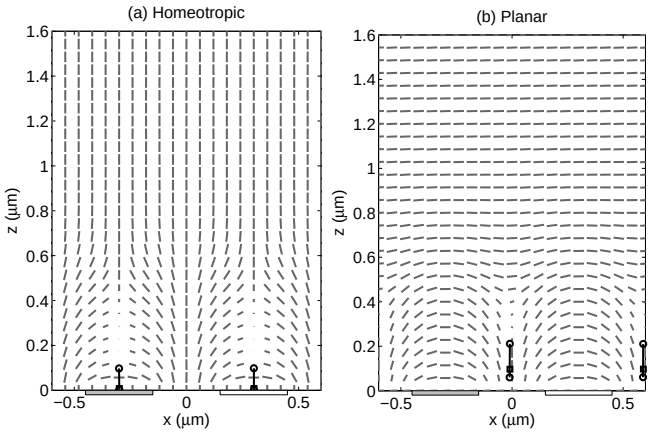

FIG. 13. Director fields obtained after $100\,\mu$s with a negative dielectric material (with properties identical to 5CB, but with $\varepsilon_\parallel$ and $\varepsilon_\perp$ swapped and flow neglected). (a) Homeotropic alignment: an applied voltage of $U_{th} = \pm 9.21\,\mathrm{V}$ induces disclinations that annihilate at 1.1 ms, leaving a HAN like orientation at steady-state. (b) Planar alignment: an applied voltage of $U_{th} = \pm 6.61\,\mathrm{V}$ induces disclinations that annihilate at 0.5 ms to leave a twisted nematic like state.

the liquid crystal orientation that results at steady-state with a $\pm 6.04\,\mathrm{V}$ voltage step applied so as to induce disclinations above both lower electrodes. At $4\,\mu$s the left hand wall undergoes pincement, whilst the right-hand wall undergoes pincement at $36\,\mu$s, after having drifted significantly towards the electrode centre.

VII. NEGATIVE DIELECTRIC ANISOTROPY MATERIALS

A negative dielectric anisotropy material with properties identical to 5CB, but with $\varepsilon_\parallel$ and $\varepsilon_\perp$ swapped has been simulated with flow neglected. For such materials, interdigitated electrodes promote in-plane reorientation of the liquid crystal. Regardless of the surface alignment, slowly ramped voltages yield in-plane orientational fields that are free of walls that might undergo pincement.

However, disclinations that appear fleetingly and annihilate inevitably can be induced by a step voltage, provided the alignment is not in-plane. Homeotropic and planar configurations have been simulated with $(\theta_0, \phi_0) = (89.9°, 89.9°)$ and $(\theta_0, \phi_0) = (2°, 0.1°)$ respectively. When a step voltage is applied a twist wall arises above the electrode centre with homeotropic alignment and between the electrodes with planar alignment. Below U_{th} the twisted region central to the wall expands laterally, giving rise to an in-plane orientational field at steady-state. Above the threshold the wall is compressed giving rise to disclination pairs, as shown in Fig. 13.

The planar case is relatively insensitive to the surface alignment. Higher pre-twists serve to increase U_{th}, but disclinations paths remain similar. Conversely, in the homeotropic case, if the surface alignment is rotated towards x it is possible to laterally shift the disclination paths. Annihilation can be then avoided by biasing the upper electrode. Ultimately, however, disclinations become pinned near the alignment layers at steady-state.

When a bias voltage is applied to the upper electrode with homeotropic alignment, the voltage threshold to create disclinations above both electrodes is $\pm 9.93\,\mathrm{V}$. The defect trajectories are almost identical to the unbiased case, but the left hand disclinations diverge to a greater extent than the right before annihilating. With a bias applied for the planar case, the threshold to create both disclination pairs is $\pm 6.72\,\mathrm{V}$. Disclination paths become curved due to the bias, but both right and left hand disclinations reach the same height enroute to annihilation.

In reality, backflow can be severe for negative materials with homeotropic alignment[44]. Dynamics are highly sensitive to the surface alignment, voltage signal and Leslie coefficients (which are less extensively characterised in the case of negative materials). Consequently, detailed consideration of this special case is beyond the scope of this paper. Nevertheless, preliminary simulations suggest that, in this configuration, backflow can lead to very high defect populations particularly when the lower electrodes are grounded and a bias is applied to the upper electrode.

VIII. VOLTAGE THRESHOLDS

Table I shows the voltage thresholds required to induce defects for homeotropic, hybrid, planar and in-plane alignments. For planar and in-plane alignments, U_{th} differs for ramped (flow independent) and stepped (flow dependent) voltage waveforms.

In reality several factors may cause the threshold voltage, U_{th}, to differ from that presented here. Firstly, the alignment layer and electrodes will be of finite thickness. A higher threshold voltage will be required to compensate

TABLE I. Voltage threshold (with no bias) for disclination formation, U_{th}, and voltage at which the free energies of wall and disclination states are equal, U_{eq}, at $(T - T^*) = -2\,\mathrm{K}$. With hybrid alignment U_{eq} is low because the bend distortion of the bulk in the wall state is lost in the defect state. Electric fields thresholds are calculated as $E_{th} = 2U_{th}/(0.3\,\mu\mathrm{m})$ and $E_{eq} = 2U_{eq}/(0.3\,\mu\mathrm{m})$.

		U_{th}(V)	E_{th}(V/μm)	U_{eq}(V)	E_{eq}(V/μm)
Homeo.		3.97	26.47	1.60	10.68
Planar	(step)	5.19	34.60	1.75	11.68
	(ramp)	5.41	36.07		
Hybrid		3.96	26.40	1.53	10.21
In-plane	(step)	5.44	36.27	1.63	10.89
	(ramp)	5.52	36.80		

for the fall-off in electric potential within the alignment layer. Secondly, thresholds are highly sensitive to the material parameters. Thirdly, the Landau-de Gennes theory is, strictly speaking, valid only in the vicinity of the nematic-isotropic phase transition. Voltage thresholds appear overestimated for temperatures further away[3]. A possible reason is that higher order moments of the order parameter may be necessary to represent the biaxial phase prior to disclination formation adequately[45].

Finally, the assumption of invariance along y is not strictly true in practice. In reality, nucleation could occur at a specific point, for instance in a region where an electrode is over-etched or where a spacer is located. Whether a wall or disclination state is favoured depends on the free energies of the two states, which depend on the applied voltage. At the voltage U_{eq} the two states are equal in energy. A voltage above U_{eq} favours the disclination state, whereas a voltage below favours the wall state. Above U_{eq}, disclination lines would 'unzip' along the line emanating from the nucleation point along y[6]. This mechanism is slower than the one considered in this paper, but results in the same steady-state.

Threshold voltages are strongly dependent on the temperature. Order parameter variations occur on a length scale defined by the correlation length[30] $\xi = \sqrt{3L_1/(2f''_B(S_0))}$. At $(T - T^*) = -2\,\mathrm{K}$, $\xi = 1.97\,\mathrm{nm}$. When the width of a wall, given by ξ_E, is similar to the correlation length, disclinations nucleate[6]. This occurs for applied voltages of $U_{th} \sim U_0 d/\xi$. At a temperature above T^* and below the clearing temperature, T_c (where the isotropic state is metastable and nematic state is stable), the correlation length is relatively large. Even low applied voltages are sufficient to reduce the order parameter and give rise to disclinations. As the temperature falls below T^* the isotropic state loses stability and the correlation length is reduced. A higher voltage is required to reduce the order and induce disclinations. For example, decreasing $(T - T^*)$ from $-2\,\mathrm{K}$ to $-4\,\mathrm{K}$ yields a 30% increase in U_{th} for homeotropic alignment and also shifts the nucleation point downwards.

An accurate expression for the temperature dependence of U_{eq} in the case of planar alignment was given by de Lózar[6]. More approximately we find that $U_{eq} \propto \ln[k(T^+ - T)]$ is a good fit for all four alignment configurations, where k is a constant and T^+ is the temperature above which the nematic phase is unstable. Decreasing $(T - T^*)$ from $-2\,\mathrm{K}$ to $-4\,\mathrm{K}$ yields a more modest 4% increase in U_{eq} for homeotropic alignment. Therefore, we expect defect formation via domain growth to be the dominant mechanism at low temperatures.

Splay or bend distortions of the liquid crystal induce a macroscopic (flexoelectric) polarisation that can alter voltage thresholds as well as the dynamic behaviour. In the homeotropic alignment case, representative flexoelectric coefficients for 5CB[46,47] of $(e_{11} + e_{33}) = -8.4\,\mathrm{pC/m}$ and $(e_{11} - e_{33}) = 7.1\,\mathrm{pC/m}$ yield defects with $U_{th} = \pm 3.94\,\mathrm{V}$. Furthermore, walls and defect trajectories become inclined. The central wall (at $x = 0$) inclines to $\theta \approx 85°$, and gives rise to a $-1/2$ defect line that follows a $\theta \approx 91.5°$ trajectory after nucleation. Walls and trajectories incline in the opposite fashion at the modelling-window edge. Lines of strength $+1/2$ migrate laterally towards the positive electrode edge. In practice, liquid crystals are switched by alternating voltage signals that, coupled with the screening effect of ionic impurities, lessen the influence of the flexoelectric polarisation.

An alternative means to induce disclinations is to ground the lower electrodes whilst applying a voltage to the upper electrode. Disclinations may only be formed in this manner for planar and in-plane cases. In these cases the nucleation point tends to the electrode edge, where the electric field is maximum. Hence, reduced electric field thresholds [given now by $E_{th} = U_{th}/(1.6\,\mu\mathrm{m})$] of $E_{th} = 8.57\,\mathrm{V}/\mu\mathrm{m}$ [$U_{th} = 13.71\,\mathrm{V}$] for planar alignment and $E_{th} = 10.78\,\mathrm{V}/\mu\mathrm{m}$ [$U_{th} = 17.25\,\mathrm{V}$] for in-plane alignment are able to induce disclinations. In the case of planar alignment, both stepped and ramped waveforms yield the same U_{th}, with the $+1/2$ lines migrating to the same position shown in Fig. 9 (a), whilst the $-1/2$ lines move laterally to the midpoint between the electrodes and to a height of 51 nm. However, for the in-plane case, disclinations only form if a stepped waveform is applied, forcing the reorienting liquid crystal to clash with the in-plane alignment. Furthermore, these disclinations annihilate, unless inhibited by applying a potential difference across the lower electrodes within $180\,\mu\mathrm{s}$.

IX. WEAK ANCHORING

In this section the effect of altering the anchoring strength, W, is considered. For the sake of simplicity, anchoring strengths in the zenithal and azimuthal directions are assumed equal, where $W_1 = W_2 = \frac{2}{3S_0}W$ in (7). In order to maintain a surface order parameter of S_0 at equilibrium[28], the coefficient a is set to $\frac{1}{6S_0}(W_1 + W_2)$.

During switching the wall that arises prior to discli-

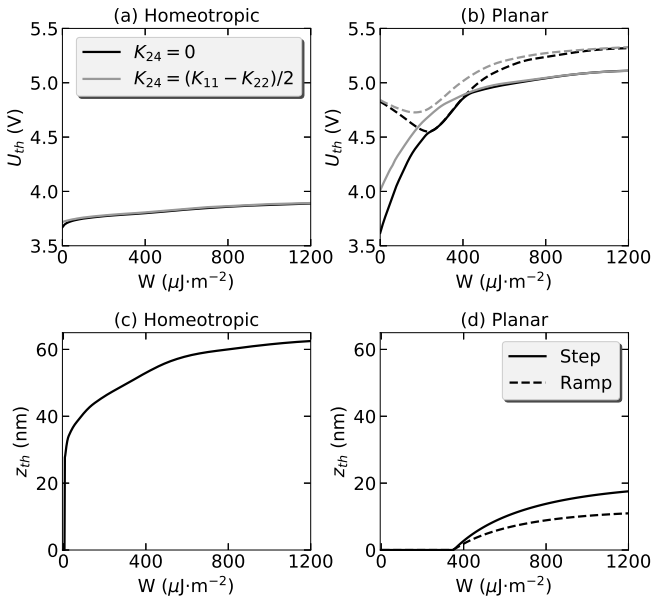

FIG. 14. Disclination formation threshold, U_{th}, as a function of anchoring strength for (a) homeotropic and (b) planar alignment. Dark lines correspond to $K_{24} = 0$, and grey lines to $K_{24} = (K_{11} - K_{22})/2$. Nucleation point height, z_{th}, as a function of anchoring strength for (c) homeotropic and (d) planar alignment with $K_{24} = 0$.

nation formation shifts downwards as the anchoring strength is reduced. Consequently, the electric field is larger at the nucleation point and a lower applied voltage will give rise to disclinations.

Figure 14 shows the voltage required to induce disclinations as a function of anchoring strength for both homeotropic and planar alignments. Additionally, the vertical position of the nucleation point, z_{th}, is given for the pertinent value of threshold voltage (z_{th} rises slightly for voltages in the excess of U_{th} for both homeotropic and planar anchoring). With homeotropic alignment the nucleation point remains in the bulk except for very weak anchoring strengths, whereas with planar alignment the nucleation point tends to the alignment layer for comparatively modest anchoring strengths.

A notable feature of Fig. 14 (b) is the turning point in the curves for weak planar alignment with ramped applied voltages. Initially, when the nucleation point tends to the surface, nucleation still converts a region of bend at the alignment layer to a region of splay. As the anchoring strength is reduced further the liquid crystal increasingly prefers to twist at the alignment layer rather than bend. A higher voltage is required to cause nucleation of the more compact twist wall, resulting in a turning point. When the applied voltage is stepped, bend persists at the alignment layer, even when the nucleation point tends to the surface, and turning points are absent.

In order to investigate the effect of K_{24} on the nucleation process, a value was chosen based on a Cauchy relation for $K_{24} = (K_{11} - K_{22})/2$, which follows from the Maier-Saupe molecular approach[48]. With homeotropic anchoring K_{24} causes a marginal upwards shift in the nucleation point and voltage threshold. This marginal effect is anticipated because the nucleation point remains in the bulk except for very weak anchoring strengths. For planar alignment the effect is more pronounced since the nucleation point tends to the surface when the anchoring strength is relatively high. Once again, a larger K_{24} reduces the tendency of the liquid crystal to twist at the alignment layer. An increased value of $K_{24} = K_{22}$ (the upper limit for positive definiteness of the free energy[48]) is found sufficient to inhibit twist entirely at the alignment layer leading to a voltage threshold that is monotonically decreasing with W.

After disclinations are induced they separate. With strong homeotropic anchoring and $\pm 3.97\,\mathrm{V}$ applied, the $+1/2$ lines become stationary 14 nm above the alignment layer. As the anchoring strength is reduced the stationary point shifts downwards. An anchoring strength of $W = 7.4 \times 10^{-4}\,\mathrm{Jm}^{-2}$ with $K_{24} = 0$ is sufficiently weak to ensure that the $+1/2$ disclinations descend all the way to the lower alignment layer. If the anchoring is weakened yet still the $+1/2$ lines smear along the alignment layer giving rise to a region of biaxial order along the alignment layer between the electrodes.

Weak anchoring affects more significantly the relaxation process. Firstly, the rate at which the $+1/2$ lines rise depends on the anchoring strength. Secondly, for weaker anchoring strengths, the ascent of the $+1/2$ lines may be delayed or inhibited entirely. However, for this to occur the applied voltage prior to relaxation must be sufficient to seat the $+1/2$ lines at the alignment layer.

With homeotropic alignment the $-1/2$ lines are immediately expelled from the lower alignment layer on relaxation if $W \geq 4.7 \times 10^{-4}\,\mathrm{Jm}^{-2}$. For weaker anchoring, the $+1/2$ lines remain stationary at first, but rise eventually when they enter the range of attraction of the descending $-1/2$ lines. For $W \leq 4.0 \times 10^{-4}\,\mathrm{Jm}^{-2}$, the $+1/2$ lines remain stationary until annihilation.

Expulsion upwards of the $+1/2$ lines converts a region of bend to splay above the alignment with homeotropic alignment. Conversely, with planar alignment, expulsion converts splay to bend. The latter is less energetically favourable, hence slightly stronger anchoring ($W \geq 5.2 \times 10^{-4}\,\mathrm{Jm}^{-2}$) is required to assure immediate expulsion.

Contrary to what one might expect, higher temperatures enlarge the biaxial regions of the alignment layer associated with the $+1/2$ lines. A high energy is associated with this biaxiality. Therefore, expulsion of the defects is energetically favourable on relaxation, unless the anchoring strength is significantly weakened.

X. SCALABILITY AND ELECTRODE PROPORTIONS

Figures 15 (a) and (b) show the effect of altering the fill factor, the proportion of the device horizontal occupied by electrode, on the threshold voltage. Recall that

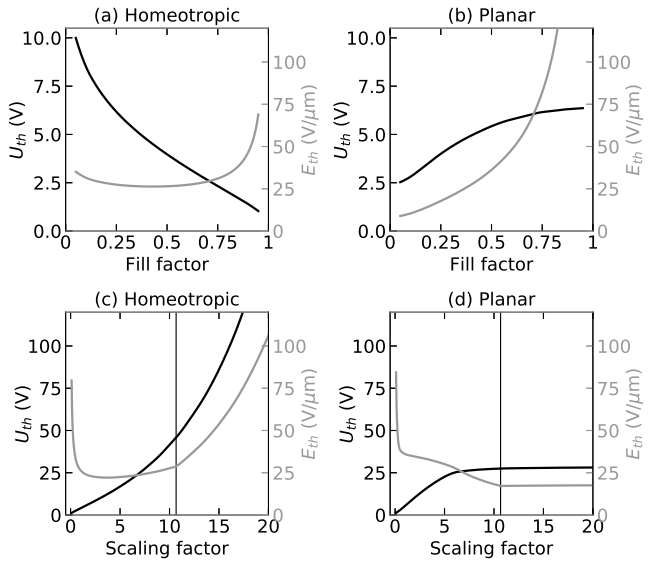

FIG. 15. Disclination formation threshold, U_{th}, as a function of (a, b) fill-factor, ν, the proportion of the device horizontal occupied by electrode; and as a function of (c, d) horizontal scaling factor, s, that multiplies the modelling-window width (with a constant cell gap of $1.6\,\mu$m and fill-factor of 0.5). Grey lines indicate electric field thresholds, E_{th}, given by (a, b) $E_{th} = 2U_{th}/[(1-\nu)\times 0.6\,\mu\text{m}]$ and (c, d) $E_{th} = U_{th}\max[2/(0.3s\,\mu\text{m}), 1/(1.6\,\mu\text{m})]$. In (c, d) vertical electric field exceeds the horizontal for $s \geq 32/3$ (marked with vertical line). For planar cases, (b, d), U_{th} corresponds to ramped voltage waveforms (stepped differ).

with homeotropic alignment the nucleation point lies in the inter-pixel gap. For large fill-factors, the inter-pixel gap is narrow and even modest voltages can give rise to an electric field at the nucleation point sufficient to induce disclinations. Hence, U_{th} in (a) exhibits a downward trend with fill-factor. However, closely spaced electrodes are more prone to short-circuits. Another factor to consider is the risk of causing dielectric breakdown of the alignment layer or liquid crystal (which occurs at $\sim 100\,\text{V}/\mu\text{m}$[49,50]). To assess this risk, the electric field threshold, E_{th}, is a more useful measure than U_{th}. For (a) and (b) it is defined as the ratio of the potential difference between the lower electrodes and the inter-pixel gap. Conversely, E_{th} begins to increase for high fill-factors due to the descent of the nucleation point towards the alignment layer. Consequently, the alignment layer becomes a stronger influence on the wall and resists pincement. For planar alignment, (b), nucleation occurs above the electrodes and is driven by the fall-off in the electric potential. Therefore, low fill factors (narrow electrodes) are conducive to disclination formation.

Figures 15 (c) and (d) show the effect of scaling the horizontal size of the modelling window on the threshold voltage. For scaling factors between 1/2 and 3, U_{th} varies linearly with scaling factor for both homeotropic and planar alignments since the effective wall height, d, is proportional to the scaling factor. Were the vertical dimension simultaneously scaled with the horizontal, this linearity would be maintained without upper limit. However, when the cell gap is fixed, the influence of the upper electrode (which is grounded) becomes apparent for scaling factors above 3. For homeotropic alignment the upper electrode serves to reduce the electric field at the nucleation point between the electrodes, leading to an increase in U_{th} for large scaling factors. For planar alignment, when the scaling factor is larger than 32/3, the electric field at the nucleation point (above the lower electrodes) is determined by the potential difference between the lower and upper electrodes and the cell gap. Consequently U_{th} becomes independent of the scaling factor.

XI. CONCLUSIONS

Fringing fields beyond a critical field strength have been shown to induce disclinations irrespective of the surface alignment for liquid crystals with positive dielectric anisotropy. Disclinations nucleate in the inter-pixel gap when alignment is normal to the substrates, and above the electrodes when alignment is tangential. Precise positional control of the disclination height is possible by adjusting the voltage across the interdigitated electrodes, whilst the lateral position may be controlled by applying a voltage bias to the upper electrode.

Weak anchoring shifts the nucleation point towards the alignment layer, a shift more evident with planar and in-plane alignments, yielding disclinations with lower voltages. Narrow electrode widths are conducive to disclination formation for planar and in-planar alignments, whereas narrow inter-pixel gaps give rise more readily to disclinations for homeotropic and hybrid alignments.

Flow of the liquid crystal serves to accelerate defect motion and perturbs their trajectories in the case of positive dielectric anisotropy materials. For negative materials, backflow can arise leading to richer transient behaviour that warrants further study.

Essentially, the devices studied herein act as programmable defect arrays and could find application as reconfigurable diffraction gratings, using defects to realise high resolution. For holographic applications, the pixel pitch determines both the viewing angle and image resolution. In order to obtain a viewing angle in excess of 30°, a pixel-pitch of $1\,\mu$m is required but, at these scales, breakdown of the driving transistor is the limiting factor when using Liquid Crystal on Silicon (LCoS) technology due to the short channel length[2]. If sub-millisecond switching is required, electrode arrays of period $< 1\,\mu$m are recommended since, when defects are present, the response time (which depends on the correlation length) increases for large defect separations[30]. Furthermore, fringing-field induced defects could prove an invaluable tool to reconfigure liquid crystal colloids. Pixel-pitches of $2-10\,\mu$m should provide adequate control, since particle trapping within defect lines has been demonstrated[21] for microspheres of diameter $1.5\,\mu$m.

ACKNOWLEDGMENTS

Authors gratefully acknowledge financial support from EPSRC (U.K.) and the Research Foundation-Flanders (FWO Vlaanderen).

AUTHOR DECLARATIONS

A. Conflicts of Interest

The authors have no conflicts to disclose.

DATA AVAILABILITY STATEMENT

The data that support the findings of this study are available from the corresponding author upon reasonable request.

[1] I. Nys, J. Beeckman, and K. Neyts, Liquid Crystals (2021), 10.1080/02678292.2021.1881831, Advance online publication.
[2] J. H. Choi, J.-H. Yang, J.-E. Pi, C.-Y. Hwang, Y.-H. Kim, G. H. Kim, H.-O. Kim, and C.-S. Hwang, Journal of the Society for Information Display **27**, 487 (2019).
[3] R. Barberi, F. Ciuchi, G. Durand, M. Iovane, D. Sikharulidze, A. Sonnet, and E. Virga, The European Physical Journal E **13**, 61 (2004).
[4] P. G. de Gennes and J. Prost, *The Physics of Liquid Crystals*, 2nd ed. (Clarendon, 1993).
[5] A. Stieb, G. Baur, and G. Meier, J. Phys. Colloques **36**, C1 (1975).
[6] A. de Lózar, W. Schöpf, I. Rehberg, D. Svenšek, and L. Kramer, Phys. Rev. E **72**, 051713 (2005).
[7] A. Vella, R. Intartaglia, C. Blanc, I. I. Smalyukh, O. D. Lavrentovich, and M. Nobili, Phys. Rev. E **71**, 061705 (2005).
[8] C. Chevallard, M. Nobili, and J. M. Gilli, Liquid Crystals **28**, 179 (2001).
[9] M. Reichenstein, H. Stark, J. Stelzer, and H.-R. Trebin, Phys. Rev. E **65**, 011709 (2001).
[10] R. Lu, X. Zhu, S.-T. Wu, Q. Hong, and T. X. Wu, Journal of Display Technology **1**, 3 (2005).
[11] R. Lindquist, J. Kulick, G. Nordin, J. Jarem, S. Kowel, M. Friends, and T. Leslie, Optics Letters **19**, 670 (1994).
[12] R. Ghannam, N. Collings, W. Crossland, R. James, S. Day, and F. A. Fernández, Proceedings of SPIE **6654** (2007).
[13] M. S. Kim, S. M. Seen, Y. H. Jung, H. Y. Kim, S. Y. Kim, K. H. Lee, Y. J. Lim, and S. H. Lee, Japanese Journal of Applied Physics **44**, 8082 (2005).
[14] A. Bhadwal, N. Mottram, A. Saxena, I. Sage, and C. Brown, Soft Matter **16**, 2961 (2020).
[15] G. Panasyuk and D. W. Allender, Journal of Applied Physics **91**, 9603 (2002).
[16] R. Ghannam, Y. Xia, D. Shen, F. A. Fernandez, H. Heidari, and V. A. L. Roy, Advanced Theory and Simulations **4**, 2100058 (2021).
[17] R. S. Zola, H. K. Bisoyi, H. Wang, A. M. Urbas, T. J. Bunning, and Q. Li, Advanced Materials **31**, 1806172 (2019).
[18] A. Habibpourmoghadam, L. Wolfram, F. Jahanbakhsh, B. Mohr, V. Y. Reshetnyak, and A. Lorenz, ACS Applied Electronic Materials **1**, 2574 (2019).
[19] S. H. Lee, S. L. Lee, and H. Y. Kim, Applied Physics Letters **73**, 2881 (1998).
[20] J. J. S. O'Neill, P. S. Salter, M. J. Booth, S. J. Elston, and S. M. Morris, Nature Communications **11**, 1 (2020).
[21] M. Škarabot, M. Ravnik, S. Žumer, U. Tkalec, I. Poberaj, D. Babič, and I. Muševič, Phys. Rev. E **77**, 061706 (2008).
[22] K. Higashiguchi, K. Yasui, M. Ozawa, K. Odoi, and H. Kikuchi, Polymer journal **44**, 632 (2012).
[23] H. Yoshida, K. Asakura, J. Fukuda, and M. Ozaki, Nature communications **6**, 1 (2015).
[24] R. You, Y.-S. Choi, M. J. Shin, M.-K. Seo, and D. K. Yoon, Advanced Materials Technologies **4**, 1900454 (2019).
[25] M. M. Genkin, A. Sokolov, O. D. Lavrentovich, and I. S. Aranson, Physical Review X **7**, 011029 (2017).
[26] L. D. Landau and E. M. Lifshitz, *Statistical Physics*, Course of Theoretical Physics; vol. 5 (Pergamon, London, 1958).
[27] A. L. Alexe-Ionescu, Physics Letters A **180**, 456 (1993).
[28] E. Willman, F. Fernández, R. James, and S. Day, Electron Devices, IEEE Transactions on **54**, 2630 (2007).
[29] T. Qian and P. Sheng, Phys. Rev. E **58**, 7475 (1998).
[30] D. Svenšek and S. Žumer, Phys. Rev. E **66**, 021712 (2002).
[31] G. Tóth, C. Denniston, and J. M. Yeomans, Phys. Rev. Lett. **88**, 105504 (2002).
[32] A. M. Sonnet, P. L. Maffettone, and E. G. Virga, Journal of Non-Newtonian Fluid Mechanics **119**, 51 (2004).
[33] R. James, E. Willman, F. A. Fernández, and S. E. Day, Electron Devices, IEEE Transactions on **53**, 1575 (2006).
[34] R. James, E. Willman, F. A. Fernández, and S. E. Day, Magnetics, IEEE Transactions on **44**, 814 (2008).
[35] A. Sonnet, A. Kilian, and S. Hess, Phys. Rev. E **52**, 718 (1995).
[36] H. J. Coles, Mol. Cryst. Liq. Cryst. Lett. **49**, 67 (1978).
[37] I. W. Stewart, *The Static and Dynamic Continuum Theory of Liquid Crystals* (CRC Press, London, New York, 2004).
[38] D. Miroshnychenko, N. A. Hill, N. J. Mottram, and J. E. Lydon, Mol. Cryst. Liq. Cryst. **437**, 251 (2005).
[39] P. G. Cummins, D. A. Dunmur, and D. A. Laidler, Mol. Cryst. Liq. Cryst. **30**, 109 (1975).
[40] P. P. Karat and N. V. Madhusudana, Mol. Cryst. Liq. Cryst. **40**, 239 (1977).
[41] H. Mori, E. C. Gartland, Jr., J. R. Kelly, and P. J. Bos, Japanese Journal of Applied Physics **38**, 135 (1999).
[42] G. Tóth, C. Denniston, and J. M. Yeomans, Phys. Rev. E **67**, 051705 (2003).
[43] C. Blanc, D. Svenšek, S. Žumer, and M. Nobili, Phys. Rev. Lett. **95**, 097802 (2005).
[44] P. J. M. Vanbrabant, J. Beeckman, K. Neyts, R. James, and F. A. Fernández, Applied Physics Letters **95**, 151108 (2009).
[45] J. P. Straley, Phys. Rev. A **10**, 1881 (1974).
[46] L. M. Blinov, M. I. Barnik, M. Ozaki, N. Shtykov, and K. Yoshino, Physical Review E **62**, 8091 (2000).
[47] F. Castles, S. Green, D. Gardiner, S. Morris, and H. Coles, Aip Advances **2**, 022137 (2012).
[48] J.-i. Fukuda, M. Yoneya, and H. Yokoyama, Phys. Rev. E **79**, 011705 (2009).
[49] H. Takanashi, J. E. Maclennan, and N. A. Clark, Japanese Journal of Applied Physics **37**, 2587 (1998).
[50] I. Dierking, Journal of Physics D: Applied Physics **34**, 806 (2001).

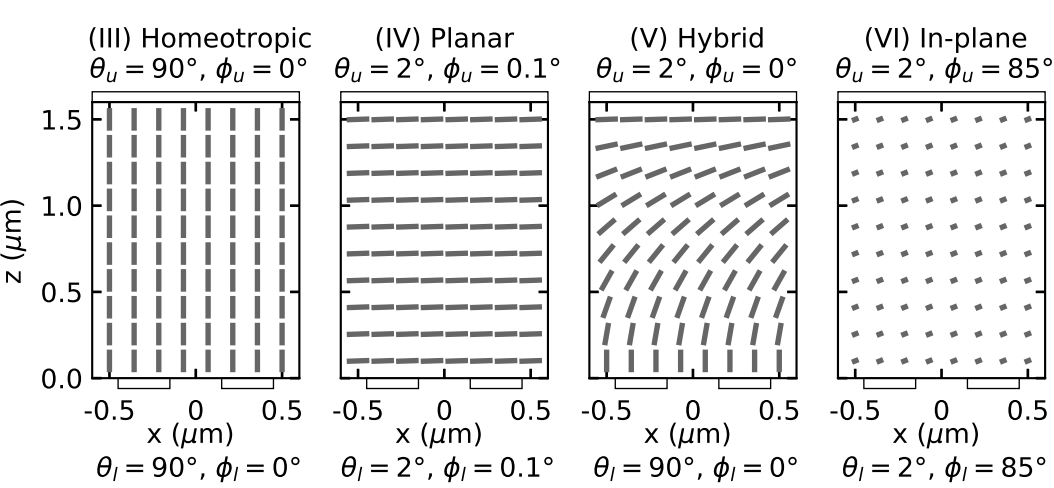
(III) Homeotropic
$\theta_u = 90°$, $\phi_u = 0°$
(IV) Planar
$\theta_u = 2°$, $\phi_u = 0.1°$
(V) Hybrid
$\theta_u = 2°$, $\phi_u = 0°$
(VI) In-plane
$\theta_u = 2°$, $\phi_u = 85°$
z (μm)
1.5
1.0
0.5
0.0
-0.5
0
0.5
x (μm)
$\theta_l = 90°$, $\phi_l = 0°$
$\theta_l = 2°$, $\phi_l = 0.1°$
$\theta_l = 90°$, $\phi_l = 0°$
$\theta_l = 2°$, $\phi_l = 85°$

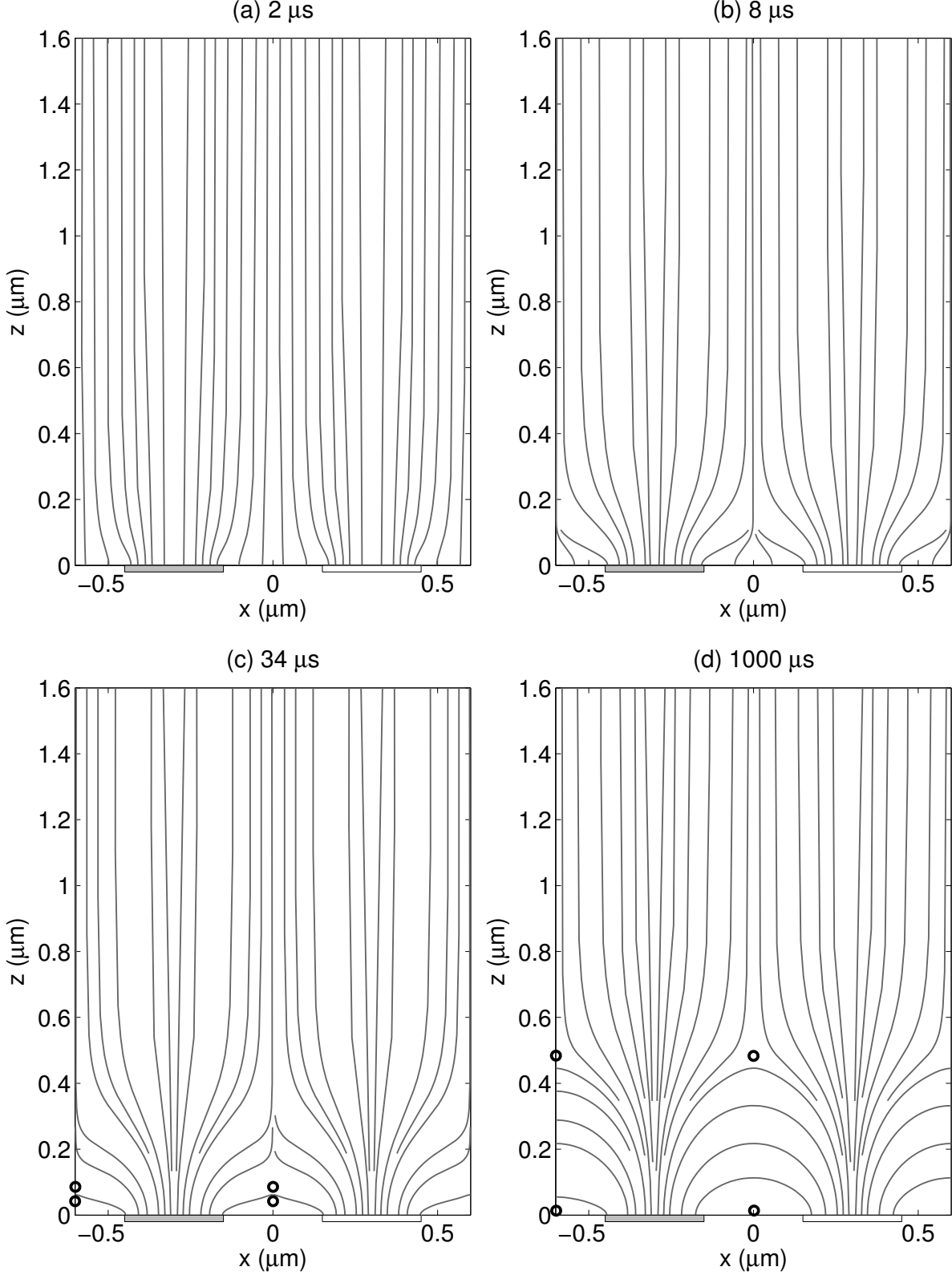
(a) 2 μs
(b) 8 μs
(c) 34 μs
(d) 1000 μs
z (μm)
x (μm)
0
0.2
0.4
0.6
0.8
1
1.2
1.4
1.6
−0.5
0
0.5

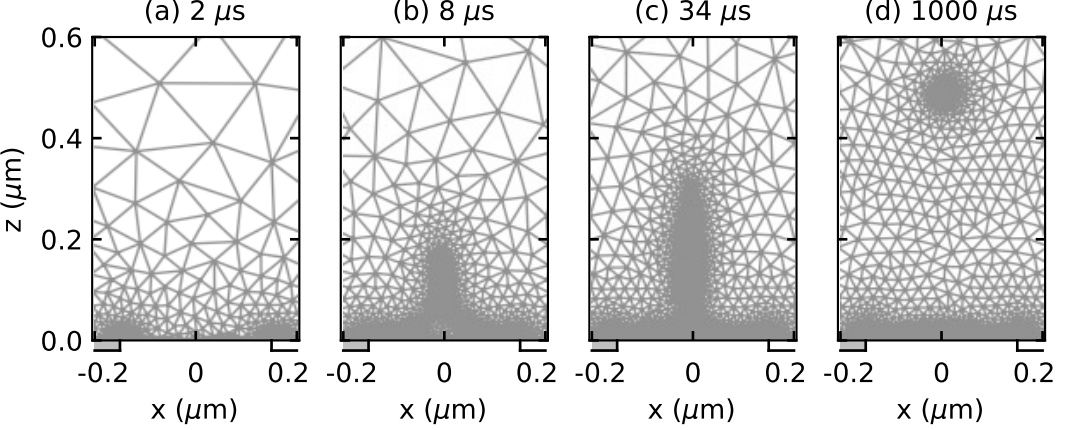
(a) 2 μs
(b) 8 μs
(c) 34 μs
(d) 1000 μs
z (μm)
0.6
0.4
0.2
0.0
-0.2
0
0.2
x (μm)

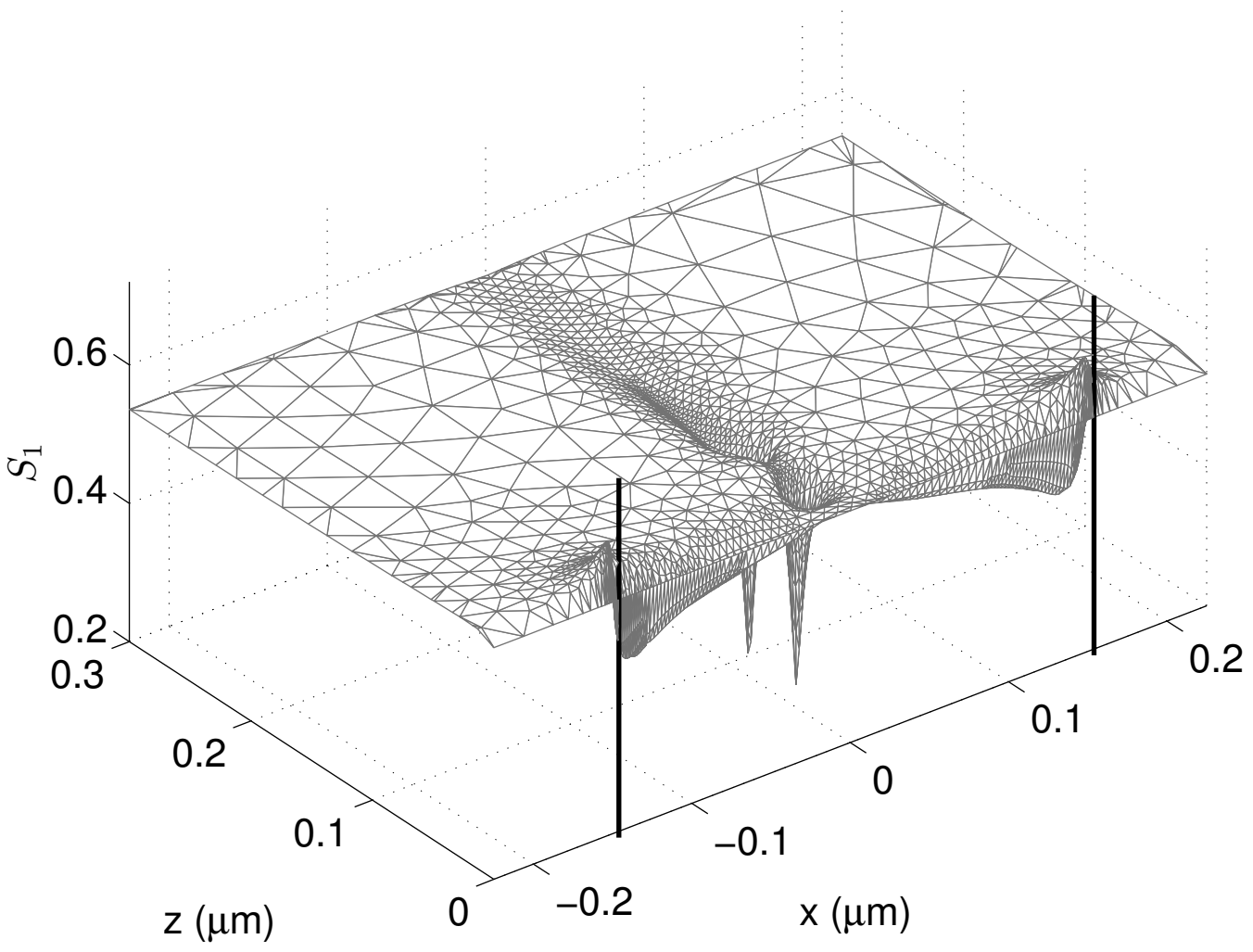
0.6
0.4
0.2
S_1
0.3
0.2
0.1
0
z (μm)
−0.2
−0.1
0
0.1
0.2
x (μm)

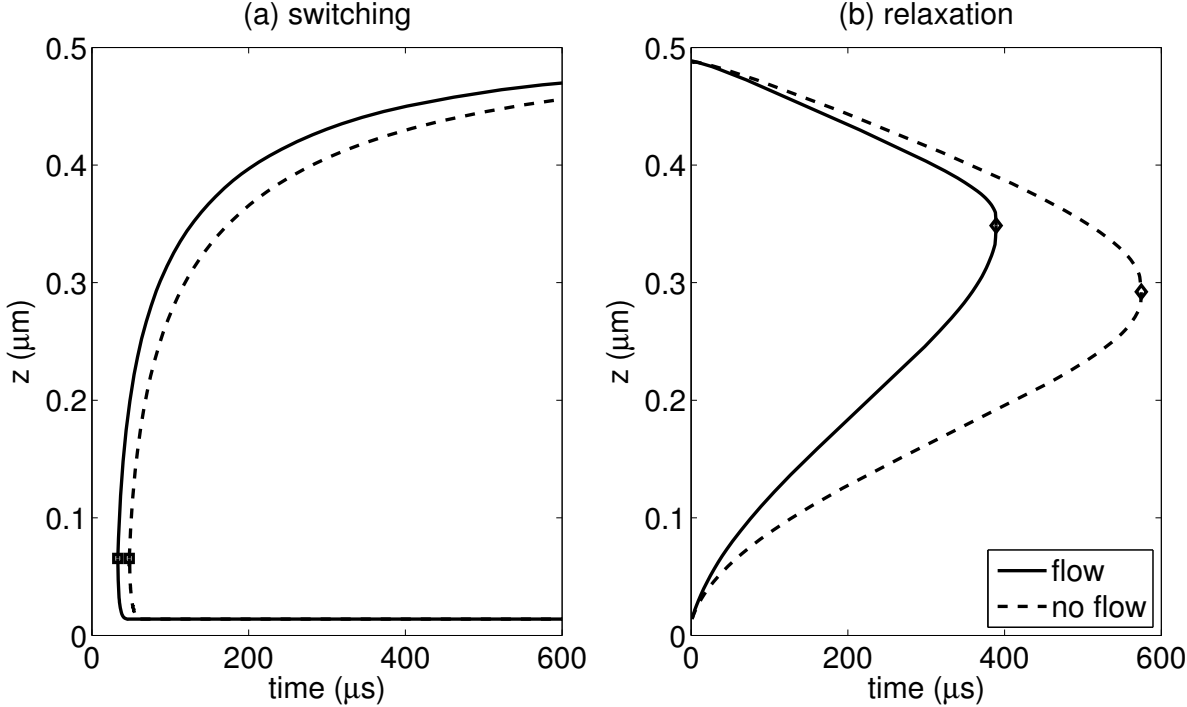
(a) switching
(b) relaxation
z (μm)
time (μs)
0
0.1
0.2
0.3
0.4
0.5
200
400
600
flow
no flow

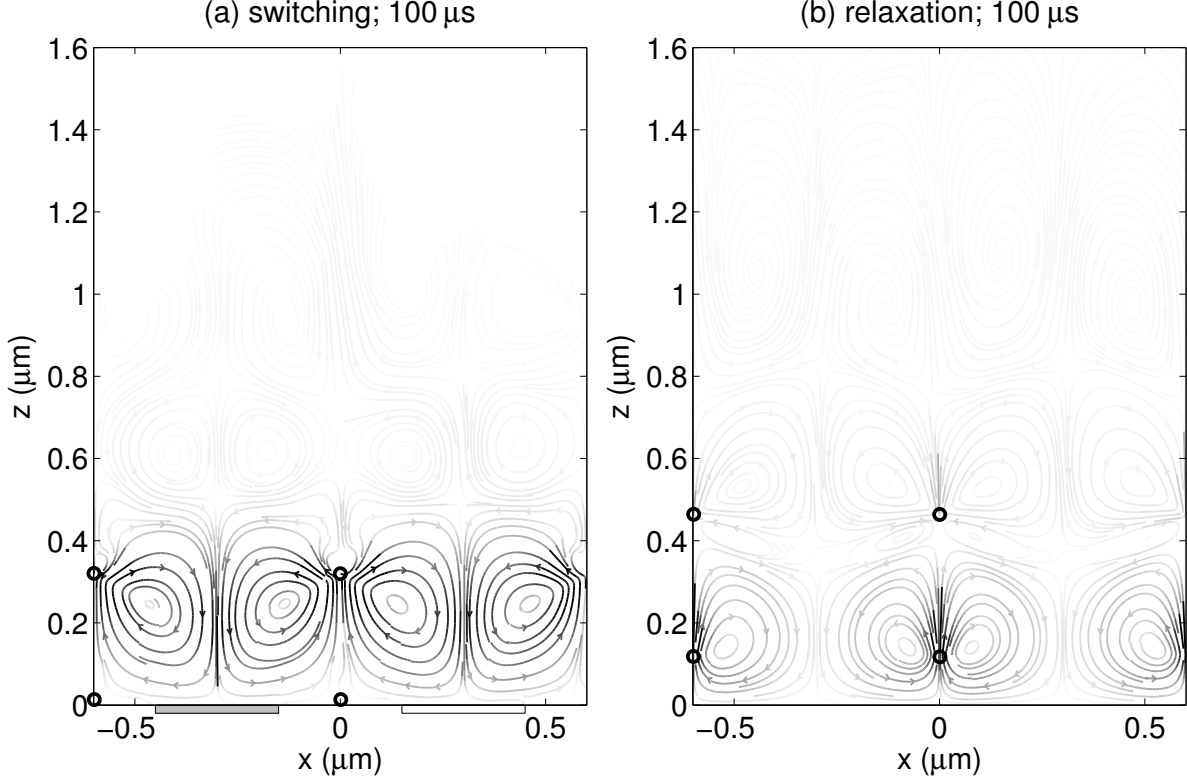
(a) switching; 100 µs
(b) relaxation; 100 µs
z (µm)
x (µm)
1.6
1.4
1.2
1
0.8
0.6
0.4
0.2
0
−0.5
0
0.5

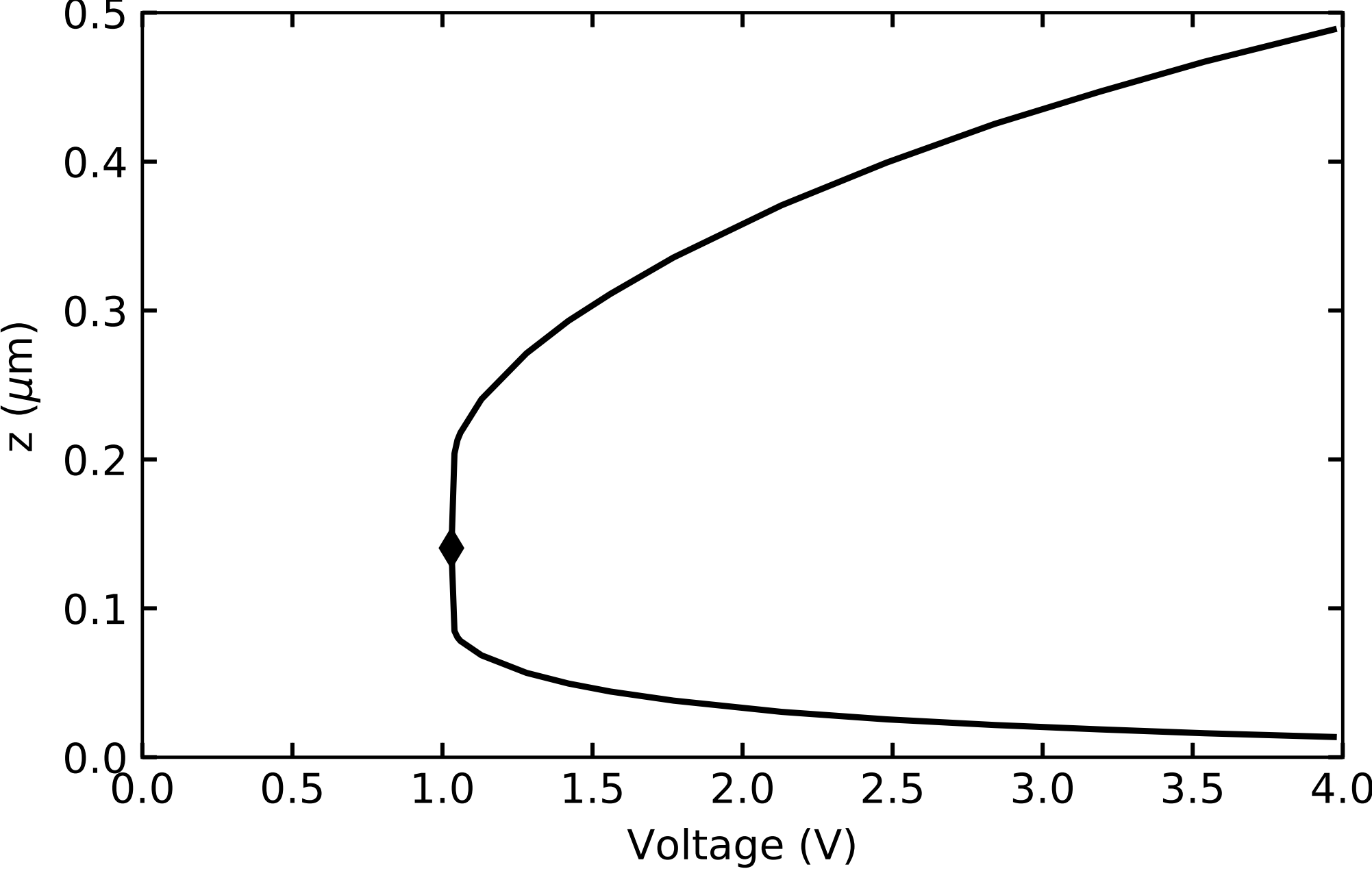
0.5
0.4
0.3
0.2
0.1
0.0
z (μm)
0.0
0.5
1.0
1.5
2.0
2.5
3.0
3.5
4.0
Voltage (V)

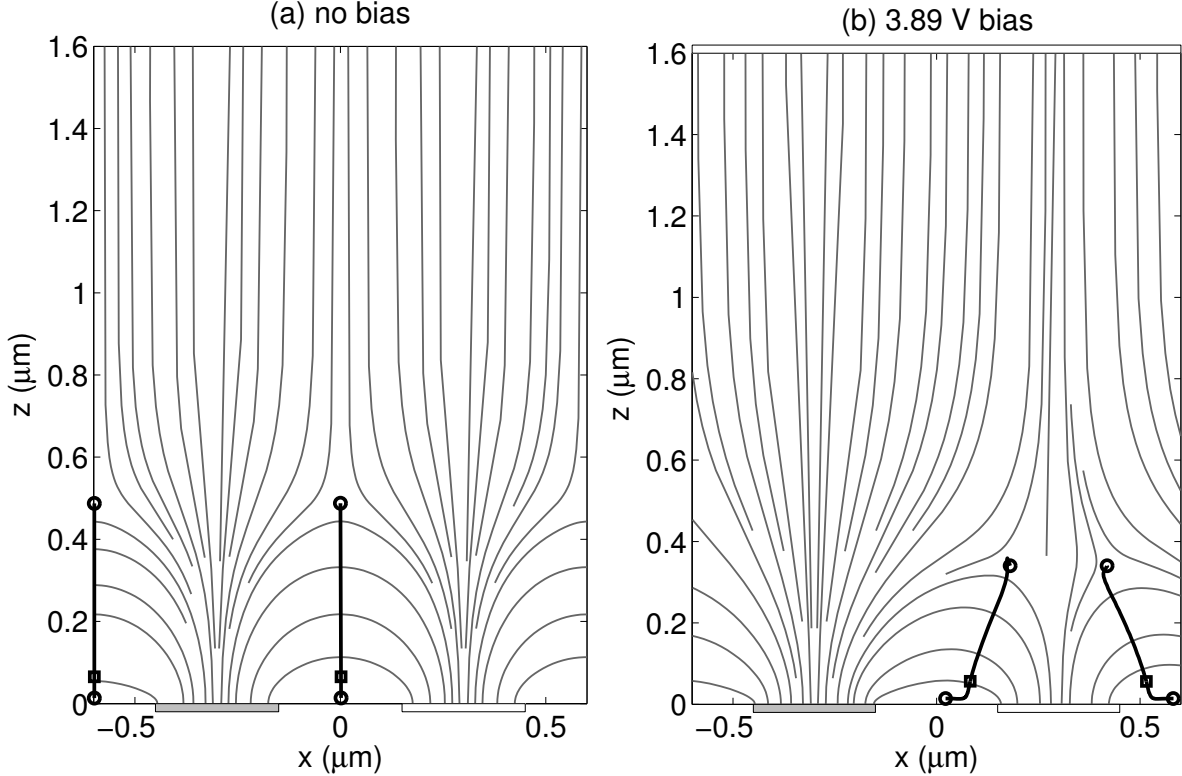
(a) no bias
(b) 3.89 V bias
z (μm)
x (μm)
1.6
1.4
1.2
1
0.8
0.6
0.4
0.2
0
−0.5
0
0.5

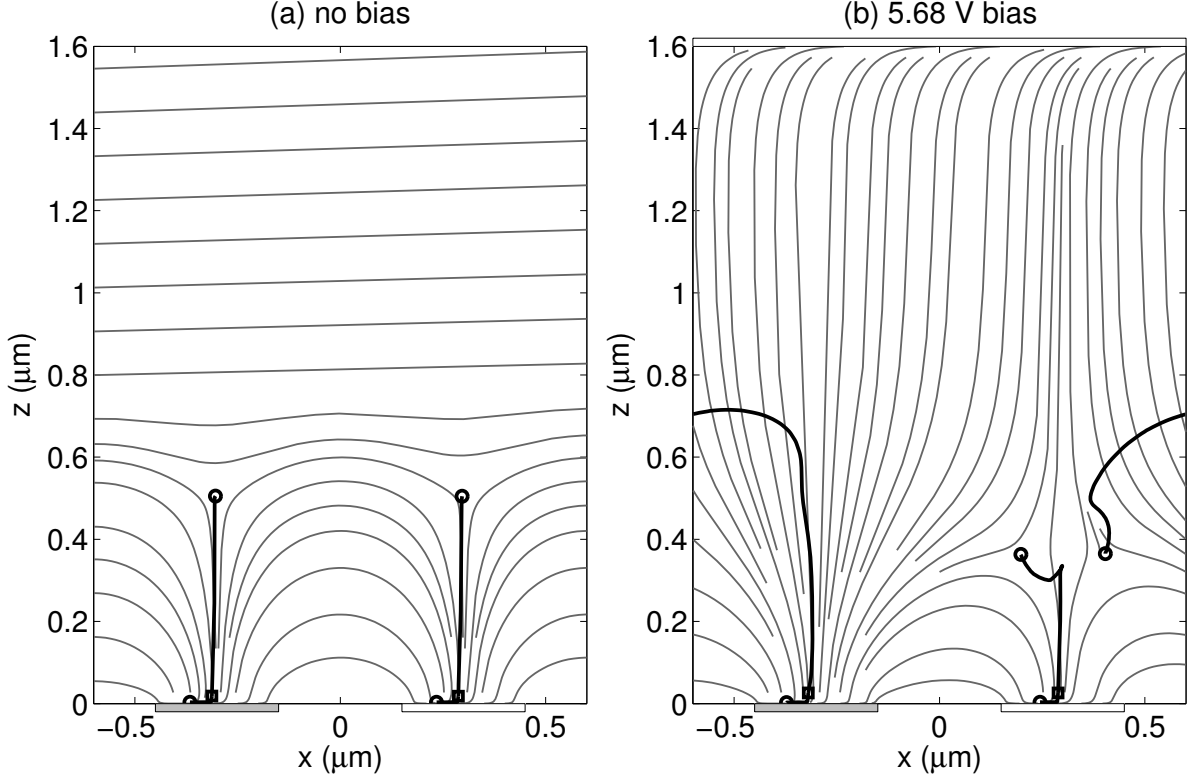
(a) no bias
(b) 5.68 V bias
z (μm)
x (μm)
1.6
1.4
1.2
1
0.8
0.6
0.4
0.2
0
−0.5
0
0.5

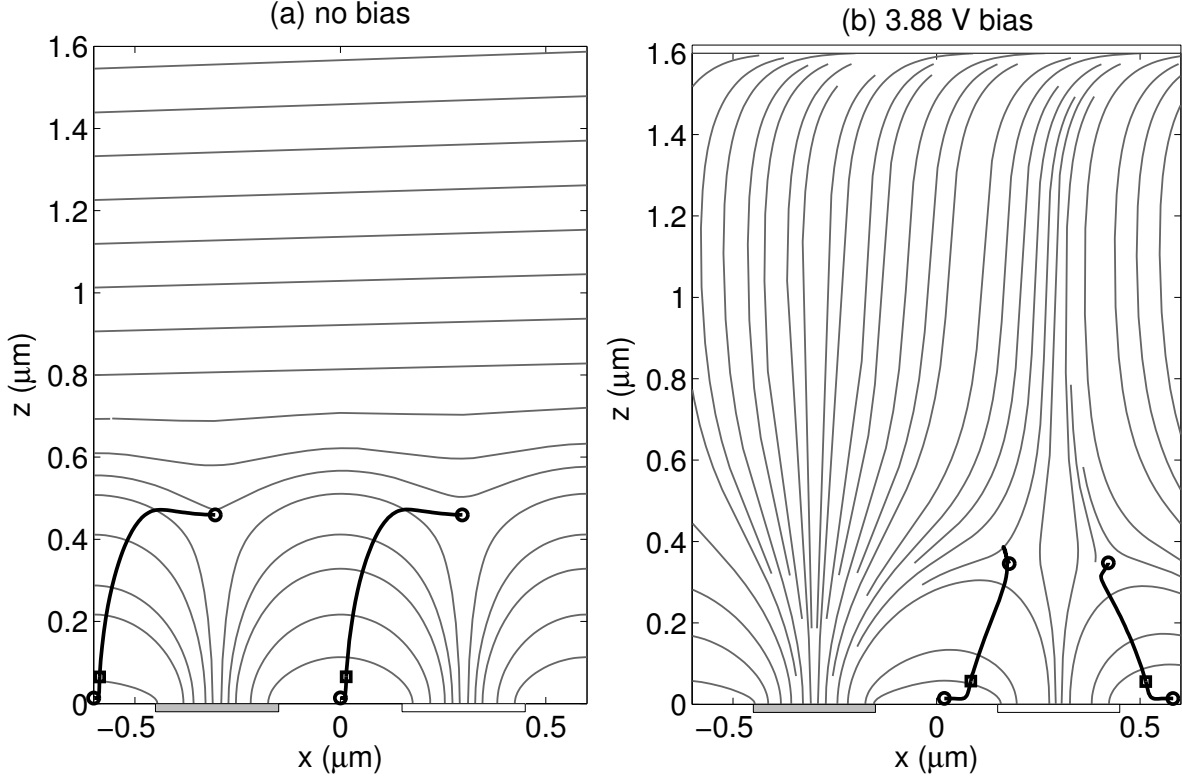
(a) no bias
(b) 3.88 V bias
z (μm)
x (μm)
1.6
1.4
1.2
1
0.8
0.6
0.4
0.2
0
−0.5
0
0.5

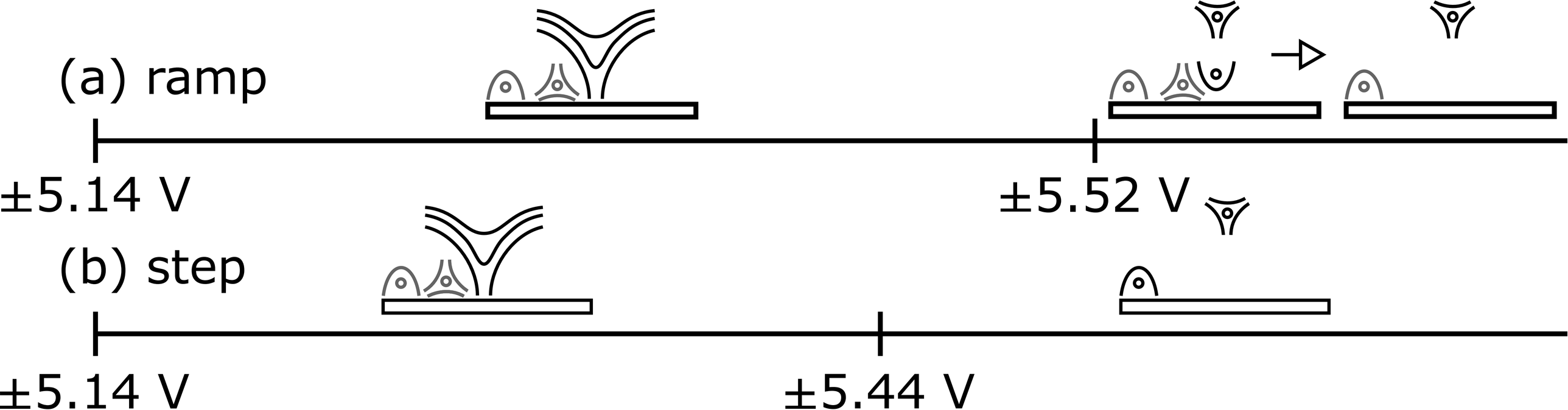
(a) ramp
±5.14 V
±5.52 V
(b) step
±5.14 V
±5.44 V

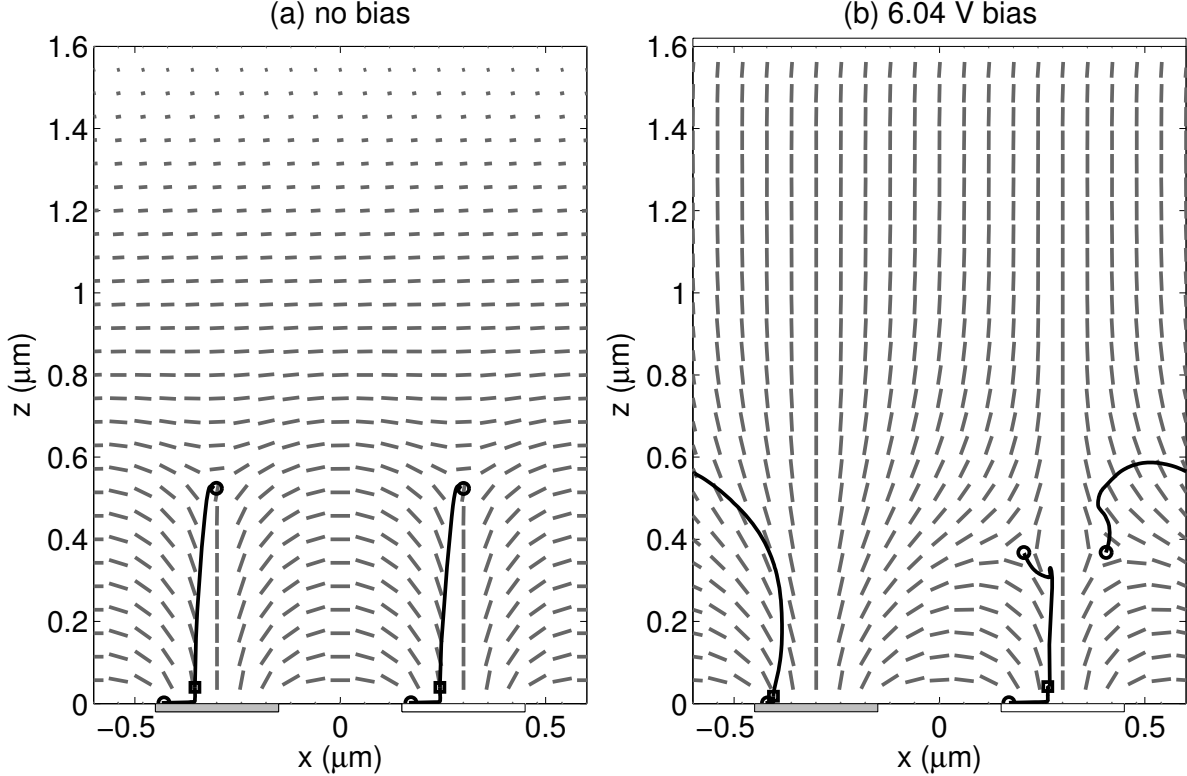
(a) no bias
(b) 6.04 V bias
z (μm)
x (μm)
1.6
1.4
1.2
1
0.8
0.6
0.4
0.2
0
−0.5
0
0.5

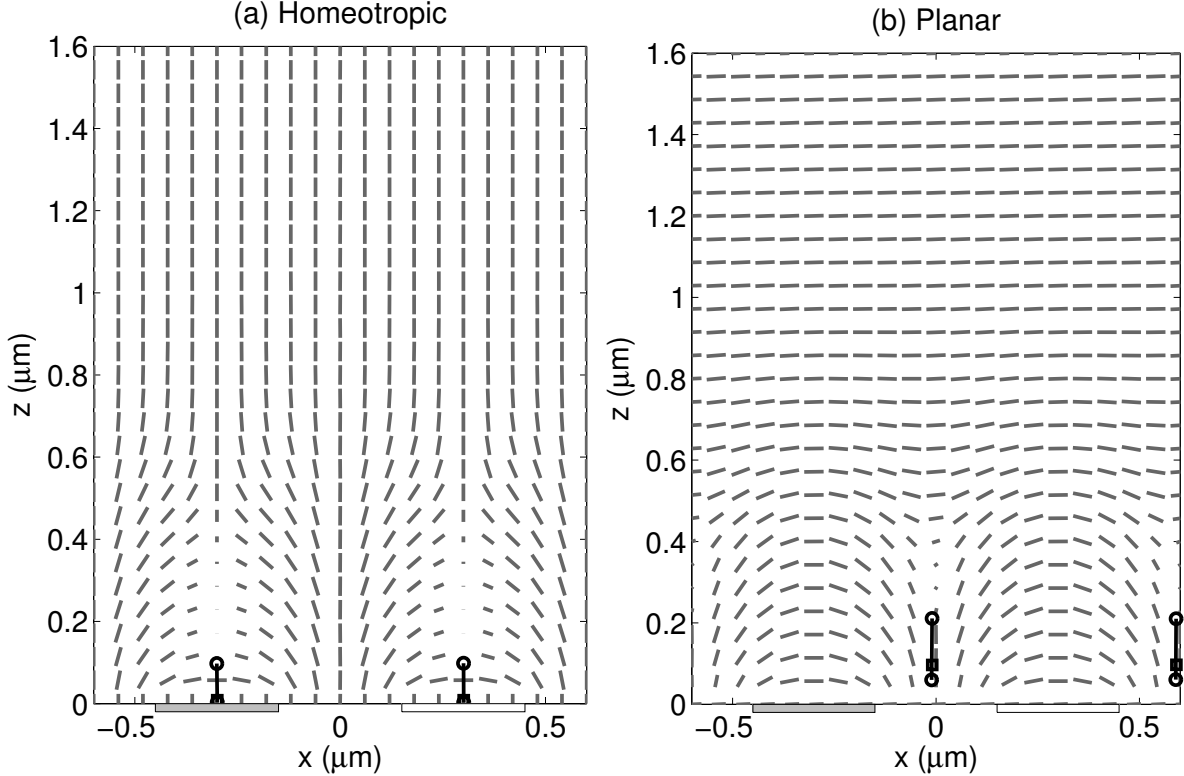
(a) Homeotropic
(b) Planar
z (μm)
x (μm)
1.6
1.4
1.2
1
0.8
0.6
0.4
0.2
0
−0.5
0
0.5

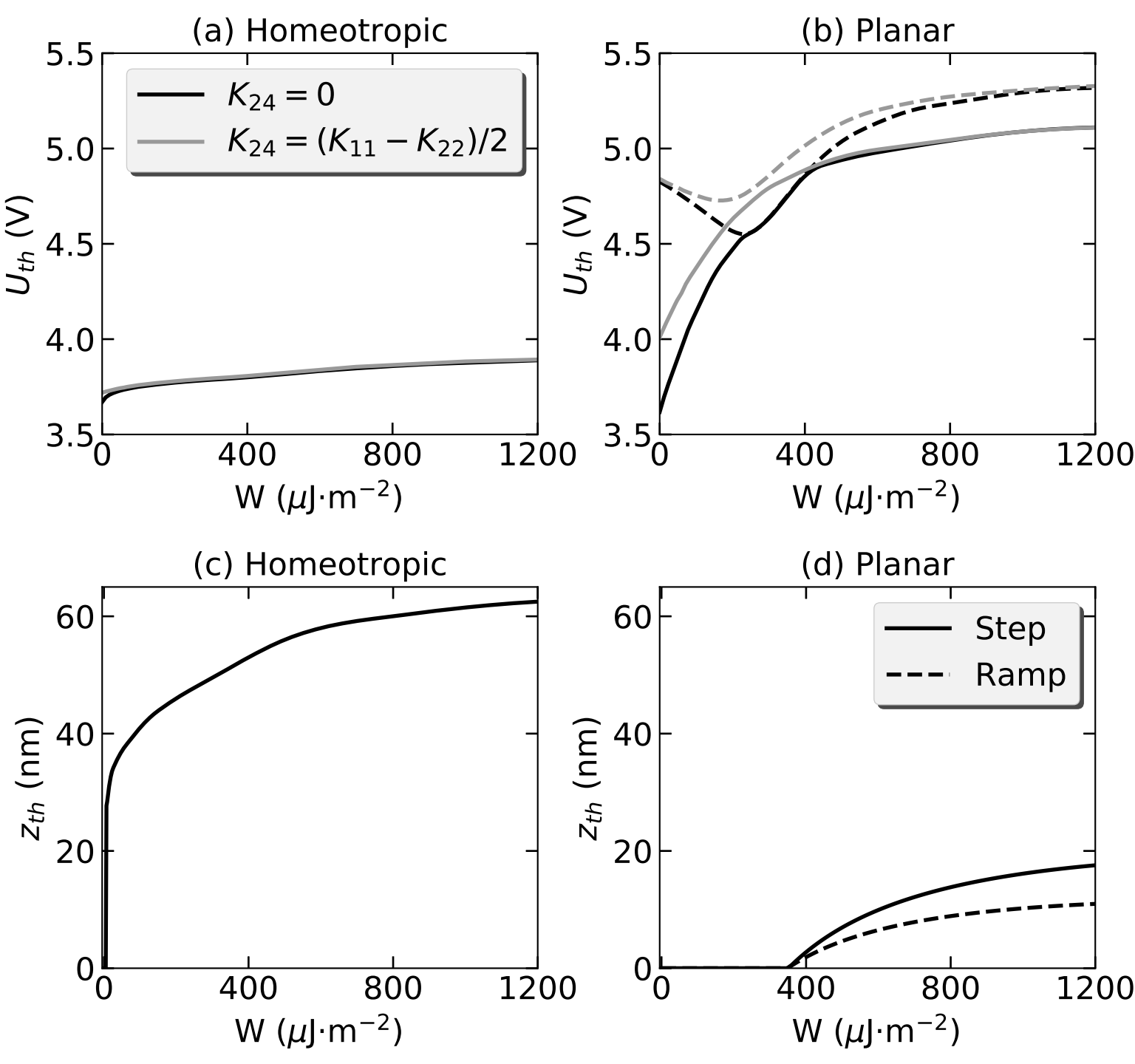
(a) Homeotropic
(b) Planar
(c) Homeotropic
(d) Planar
$K_{24} = 0$
$K_{24} = (K_{11} - K_{22})/2$
Step
Ramp
U_{th} (V)
z_{th} (nm)
W (μJ·m^{-2})
0
400
800
1200
3.5
4.0
4.5
5.0
5.5
20
40
60

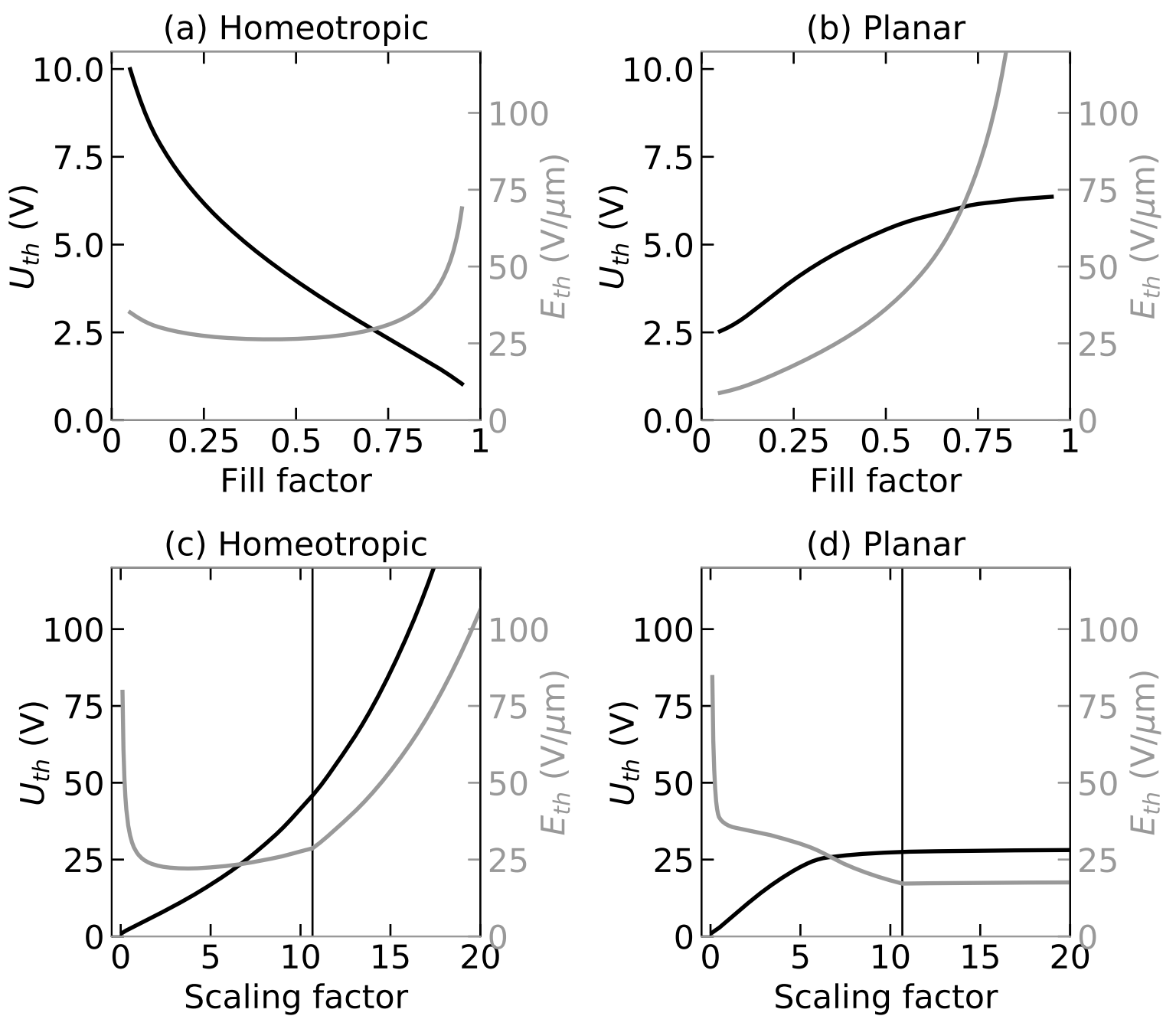
(a) Homeotropic
(b) Planar
(c) Homeotropic
(d) Planar
U_{th} (V)
E_{th} (V/μm)
Fill factor
Scaling factor
0.0
2.5
5.0
7.5
10.0
0
25
50
75
100
0.25
0.5
0.75
1
5
10
15
20